

## Durham E-Theses

---

### *Kinetics of CVD graphene growth on polycrystalline copper and the influence of surface texture*

TALMANTAITE, ALINA

#### How to cite:

---

TALMANTAITE, ALINA (2018) *Kinetics of CVD graphene growth on polycrystalline copper and the influence of surface texture*, Durham theses, Durham University. Available at Durham E-Theses  
Online: <http://etheses.dur.ac.uk/12792/>

#### Use policy

---

The full-text may be used and/or reproduced, and given to third parties in any format or medium, without prior permission or charge, for personal research or study, educational, or not-for-profit purposes provided that:

- a full bibliographic reference is made to the original source
- a [link](#) is made to the metadata record in Durham E-Theses
- the full-text is not changed in any way

The full-text must not be sold in any format or medium without the formal permission of the copyright holders.

Please consult the [full Durham E-Theses policy](#) for further details.

# Kinetics of CVD graphene growth on polycrystalline copper and the influence of surface texture

Alina Talmantaite

**Abstract:** Graphene growth kinetics have been studied with the aim of investigating two incompatible models which have been applied in the recent literature – a modified Johnson-Mehl-Avrami-Kolmogorov (JMAK) model and a modified Gompertz function. Graphene was grown by atmospheric pressure chemical vapour deposition (APCVD) at 1065°C on polycrystalline copper foil substrates and film growth as a function of time was studied by scanning electron microscopy (SEM). The graphene coverage with time was found to evolve sigmoidally, preventing a superficial differentiation between the two models. However, further analysis demonstrated that the modified JMAK model was incorrect due to a non-constant Avrami exponent and general incompatibility of the model assumptions with the physical nature of graphene growth by CVD. The Gompertz model was found to match the coverage data fairly well; however there are still some questions regarding the applicability of this model, the reasons for which are discussed.

SEM micrographs demonstrate that certain copper grains supported selective nucleation and anisotropic growth of graphene domains at low densities, while nucleation was homogeneous and of fairly high density on other grains. These differences in nucleation and island morphology were amplified in samples grown at a lower temperature (1025°C), including formation of graphene domain chains on certain grains. Electron backscattering diffraction (EBSD) was employed to characterise the copper surface texture, which revealed that chains of islands form on step bunches present on very rough grains with orientations close to (111). Analysis of graphene coverage on different copper faces was carried out, which showed that the coverage remained approximately constant over the surface of a sample grown at high temperature, while growth at a lower temperature resulted in a decreasing coverage on grains with an increasing fraction of (111) terraces. Potential reasons for these orientation-dependent differences in graphene growth are discussed.

# Kinetics of CVD graphene growth on polycrystalline copper and the influence of surface texture

Alina Talmantaite

A Thesis presented for the degree of  
Master of Science by Research



Department of Physics  
Durham University  
United Kingdom

September 2018

# Contents

<b>Abstract</b>	<b>1</b>
<b>List of Figures</b>	<b>iii</b>
<b>1 Introduction</b>	<b>1</b>
1.1 Graphene: Introduction . . . . .	1
1.2 Structure and properties of graphene . . . . .	2
1.3 Synthesis of graphene . . . . .	5
1.3.1 Exfoliation techniques . . . . .	5
1.3.2 "Bottom-up" growth . . . . .	8
1.4 Kinetics of graphene growth by CVD . . . . .	9
1.5 Organisation of thesis . . . . .	13
1.6 Summary . . . . .	13
<b>2 Experimental techniques</b>	<b>14</b>
2.1 Raman scattering . . . . .	14
2.1.1 Introduction . . . . .	14
2.1.2 Origin of Raman scattering . . . . .	15
2.1.3 Complementarity of Raman and infrared spectra . . . . .	16
2.1.4 Raman spectrum of graphene . . . . .	18
2.2 Scanning electron microscopy . . . . .	21
2.2.1 Introduction . . . . .	21

---

2.2.2	Electron-specimen interactions . . . . .	21
2.2.3	Imaging with secondary electrons . . . . .	22
2.2.4	Backscattered electrons and their diffraction . . . . .	23
2.2.5	Design of a scanning electron microscope . . . . .	25
2.3	Chemical vapour deposition . . . . .	26
2.3.1	Introduction . . . . .	26
2.3.2	The CVD Process . . . . .	28
2.3.3	CVD of graphene on copper substrates using methane . . . . .	29
2.3.4	CVD systems . . . . .	31
2.3.5	Summary . . . . .	33
<b>3</b>	<b>Experimental instrumentation and sample preparation</b>	<b>34</b>
3.1	CVD system for graphene growth . . . . .	34
3.2	ASEQ Instruments Rm1 Raman spectrometer . . . . .	35
3.3	FEI Helios Nanolab 600 DualBeam system . . . . .	35
3.4	Sample preparation . . . . .	38
3.5	Summary . . . . .	40
<b>4</b>	<b>The kinetics of graphene growth on copper and its influence on island morphology</b>	<b>41</b>
4.1	Introduction . . . . .	41
4.2	Experimental . . . . .	43
4.3	Results and discussion . . . . .	45
4.3.1	Characterisation of graphene samples . . . . .	45
4.3.2	The kinetics of graphene growth . . . . .	48
4.3.3	Influence of copper morphology on the graphene growth . . . . .	54
4.4	Summary . . . . .	59
<b>5</b>	<b>Summary and further work</b>	<b>62</b>
5.1	Summary . . . . .	62
5.2	Further work . . . . .	63

# List of Figures

1.1	A sheet of graphene. . . . .	1
1.2	Unit cell of graphene lattice. . . . .	3
1.3	The band structure of graphene. . . . .	3
1.4	Top-down methods for graphene production. . . . .	6
1.5	Bottom-up methods for graphene production. . . . .	8
1.6	Site-saturate graphene growth model (a) and a modified JMAK equation fitting to the graphene growth data obtained by Kim <i>et al.</i> . . . . .	11
1.7	A modified Gompertz equation fitting to the graphene growth data obtained by Celebi <i>et al.</i> . . . . .	13
2.1	Rayleigh, Stokes and anti-Stokes scattering mechanisms involving real states $J=0, 2$ and virtual states $V_0$ and $V_1$ . . . . .	16
2.2	Non-resonant and resonant Raman (Stokes) scattering mechanisms involving ground electronic states and virtual states $V_1$ and $V_2$ . . . . .	17
2.3	Raman spectrum of graphene taken with a 2.41 eV laser excitation energy. . .	19
2.4	Phonon dispersion relation of monolayer graphene arising from iLO, iTO, oTO, iLA, iTA and oTA vibrational modes . . . . .	19
2.5	Resonant Raman scattering process generating $G$ band (a) and doubly resonant Raman scattering process generating $2D$ and $D$ bands. . . . .	20
2.6	A schematic of signals produced by scattering events between an incident electron beam and a specimen. . . . .	22
2.7	The origins of contrast difference in SEM imaging. . . . .	23
2.8	The electron backscattering mechanism and pattern formation. . . . .	25

---

2.9	A schematic of an SEM construction. . . . .	27
2.10	A schematic of the stages in CVD growth of thin films. . . . .	28
2.11	SEM images of graphene islands grown at low pressures (a), (b) and atmospheric pressure (c). . . . .	31
2.12	A scheme of a vertical cold-wall CVD reactor (a) and a horizontal hot-wall reactor. . . . .	32
3.1	CVD system used for graphene growth. . . . .	35
3.2	ASEQ Instruments Rm1 Raman spectrometer used for graphene characterisation. . . . .	36
3.3	FEI Helios Nanolab 600 DualBeam system. . . . .	36
3.4	Imaging (a) and EBSD (b) in FEI Helios Nanolab 600 DualBeam system. . . . .	37
3.5	Forward scattered electron images and EBSD maps of Cu surface before and after the treatment. . . . .	39
3.6	Graphene growth cycle. . . . .	40
4.1	Graphene islands on Cu. . . . .	43
4.2	Differences in island growth on different Cu faces. . . . .	44
4.3	Graphene coverage evolution with time, (a), and SEM micrographs of graphene domains grown under a stream of CH <sub>4</sub> for 60 s, (b), 67 s, (c), 80 s, (d), and 87 s, (e). . . . .	46
4.4	Raman spectrum of as-grown graphene. The red lines shows a Lorentzian fit to the 2D peak. . . . .	47
4.5	Evolution of intensity ratios I <sub>D</sub> /I <sub>G</sub> and I <sub>2D</sub> /I <sub>G</sub> . . . . .	48
4.6	The shapes of Raman 2D band of 1-4 layer graphene and HOPG. . . . .	49
4.7	Graphical representation of equation 4.3.1, (a), and its inverse, (b). . . . .	50
4.8	Modified JMAK (green) and modified Gompertz (red) model fitting to the coverage data obtained from the as-grown samples. . . . .	51
4.9	Linearised JMAK model for graphene growth. The red line represent the best linear fit. . . . .	52
4.10	Gompertz model fitting to the growth data defined by the JMAK model. . . . .	53

---

4.11 Morphological differences of graphene islands grown on different Cu grains. . .	55
4.12 Graphene island nucleation along Cu steps. . . . .	56
4.13 Secondary electron image of Cu surface, (a), and an EBSD map superimposed with a forward scattered electron image of the same area, (b). . . . .	57
4.14 SEM images of anisotropic graphene growth along the steps of Cu(111) surface at CH <sub>4</sub> exposure times of 20 min, (a), and 65 min . . . . .	58
4.15 Graphene ribbon formation on Cu during LPCVD. . . . .	58
4.16 Graphene coverage of a sample grown at 1065°C with respect to a fraction of (100), (110) and (111) surfaces that high Miller index grains are composed of, (a), (b) and (c) respectively. Lines are a guide to the eye. . . . .	60
4.17 Graphene coverage of a sample grown at 1025°C with respect to a fraction of (100), (110) and (111) surfaces that high Miller index grains are composed of, (a), (b) and (c) respectively. Lines are a guide to the eye. . . . .	61

# Declaration

The work in this thesis is based on research carried out in the Department of Physics, Durham University, United Kingdom. No part of this thesis has been submitted elsewhere for any other degree or qualification and it is all my own work unless referenced to the contrary in the text.

**Copyright © September 2018 by Alina Talmantaite.**

“The copyright of this thesis rests with the author. No quotations from it should be published without the author’s prior written consent and information derived from it should be acknowledged.”

# Acknowledgements

I would like to thank my supervisor, Dr Michael R. C. Hunt, for his guidance, patience and invaluable experience I have gained working with him.

I am also grateful to Mr Leon Bowen for his help with SEM and EBSD measurements.

I am thankful to the technical and IT staff in the Department of Physics, who were always there to solve frequent technical problems.

I am especially grateful to my housemate, Behzad, for his moral support and comforting words at my most miserable moments.

Finally, I would like to thank my parents, who made my dreams possible.

# Chapter 1

## Introduction

This chapter gives an introduction to the structure of graphene, its electronic and mechanical properties, and emerging applications. A variety of graphene production techniques are discussed, including a number of graphite exfoliation methods, growth on SiC, molecular beam epitaxy (MBE) and chemical vapour deposition (CVD). Two opposing kinetic models for graphene growth are outlined providing the motivation for the work presented in this thesis.

### 1.1 Graphene: Introduction

Graphene – an atomically-thin quasi-two-dimensional (2D) solid consisting of a hexagonal grid of carbon atoms, as illustrated in Fig. 1.1 – has been studied as an integral part of graphitic materials since the 1940s [1]. It was long believed that this material could not exist in isolation based on the Mermin-Wagner theorem, which states that at finite temperatures

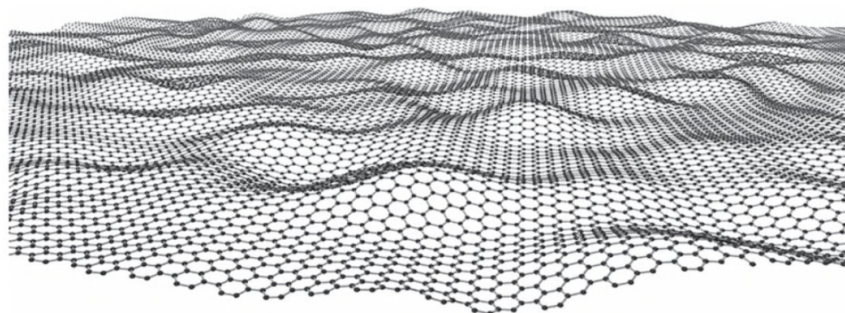


Figure 1.1: A sheet of graphene.

thermal displacements arising in 2D materials would be comparable to interatomic distances and therefore would destroy long-range crystalline order [2]. However, in 2004 the first conclusively identified free-standing graphene sample was produced by Novoselov and Geim [3]. Interestingly, it did not violate the Mermin-Wagner theorem: lateral rippling of the sample in the third dimension suppressed thermal vibrations and hence stabilised the graphene membrane [4]. This discovery led to Novoselov and Geim receiving the Nobel Prize for Physics in 2010 and initiated intensive studies of graphene and related 2D materials such as monolayers of transition metal dichalcogenides (MoS<sub>2</sub>, WSe<sub>2</sub>, etc.) [5] and 2D allotropes of chemical elements like germanium [6], silicon [7] and phosphorus [8].

## 1.2 Structure and properties of graphene

The building block of graphene is the carbon atom, which has an excited-state electron configuration of [He] 2s<sup>1</sup> 2p<sup>3</sup>. In a hexagonal arrangement, each carbon atom has three nearest neighbours to which it is linked by strong, in-plane  $\sigma$  bonds [9] of the length of 1.42 Å. These bonds are positioned at 120° angles to one another and arise due to 2s, 2p<sub>x</sub> and 2p<sub>y</sub> orbital hybridization [10]. The remaining p<sub>z</sub> electron contributes to the formation of the  $\pi$  bond, which has a node in the graphene plane. The overlap of neighbouring  $\pi$  bonds creates a delocalised "cloud" of electrons above and below the atomic plane.

Graphene has a hexagonal unit cell containing two non-equivalent atoms originating from two interspersed triangular sublattices, A and B, which are related to each other by inversion symmetry (Fig. 1.2). Considering the nearest neighbour tight-binding model, which assumes that only the low energy  $\pi$  electrons contribute to the electronic properties of graphene, the Schrödinger equation can be solved to obtain the electron energy dispersion relation

$$E(k_x, k_y) = \pm\gamma_0 \sqrt{1 + 4 \cos \frac{\sqrt{3}k_x a}{2} \cos \frac{k_y a}{2} + 4 \cos^2 \frac{k_y a}{2}}, \quad (1.2.1)$$

where,  $k_x$  and  $k_y$  are the components of the electron wavevector,  $k$ ,  $\gamma_0$  is the nearest neighbour overlap integral and  $a = \sqrt{3}a_{C-C}$  with  $a_{C-C}$  corresponding to the carbon-carbon distance [11]. The band structure produced by this dispersion relationship in the extended hexagonal Brillouin zone is depicted in Fig. 1.3. It is evident that the overlap of the  $\pi$  bonds generates two bands: bonding or valence band,  $\pi$ , and antibonding or conduction band,  $\pi^*$ . They are symmetric with respect to the  $E(k_x, k_y) = 0$  plane and are degenerate at the high symmetry points  $K$  and  $K'$ , which are located at six corners of the Brillouin zone and originate from

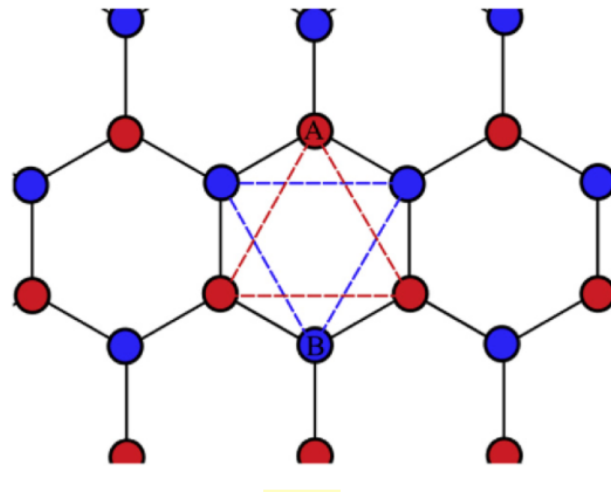


Figure 1.2: Unit cell of graphene lattice, where A and B denote two inversely symmetrical triangular sublattices [11].

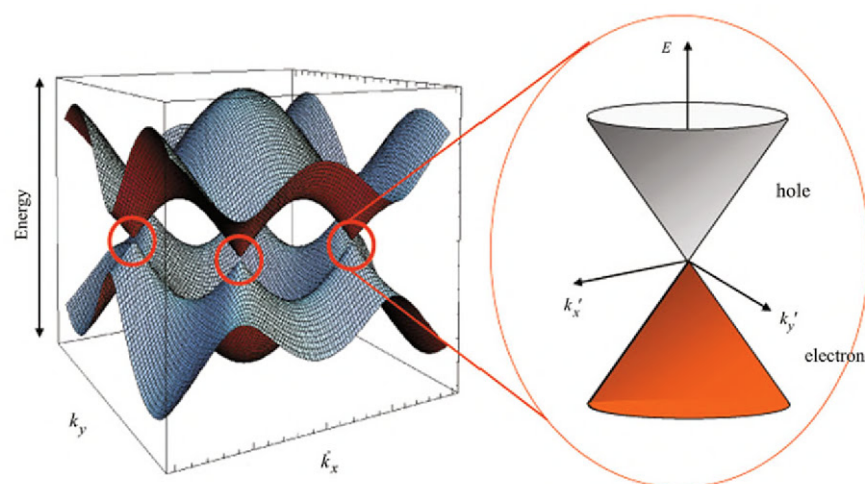


Figure 1.3: The band structure of graphene [12]. Near high symmetry  $K$  and  $K'$  points (marked by circles), the dispersion relation is linear with the valence and conduction bands taking conic shapes.

electrons associated with sublattice points A and B respectively. At absolute zero, the Fermi surface of intrinsic graphene is a point surface which coincides with the degeneracy points  $K$  and  $K'$ ; therefore, graphene can be referred to as a zero-gap semiconductor or a semimetal with no band overlap.

One of the most interesting electronic properties of pristine graphene arises from both the geometry and electronic states of  $\pi$  and  $\pi^*$  bands near their intersection points. While for typical metals and semiconductors the dispersion relationship at the band edges can be approximated by a quadratic function, the dispersion relationship for graphene at low energies is linear, resulting in valence and conduction bands taking conic shapes and meeting at the degeneracy point (also known as the Dirac point) as shown in the inset of Fig. 1.3. Here, the interaction between electrons and the periodic graphene lattice potential gives rise to quasiparticles which behave like massless Dirac fermions and move at an effectively relativistic Fermi velocity  $v_F \approx 10^6 \text{ m s}^{-1}$ . Furthermore, the electronic states of these quasiparticles can be understood as a superposition of electronic states associated with graphene sublattices A and B. Hence, their wavefunctions consist of two components, introducing the notion of a pseudospin due to its similarity to quantisation of the  $z$ -component of the electron spin [4]. Due to graphene's band structure, the rotation of the pseudospin by  $2\pi$  gives the Berry's phase of  $\pi$ , which leads to unusual quantum effects such as a half-integer shift in the quantum Hall effect, Klein tunnelling, as well as suppression of electron backscattering between  $K$  and  $K'$  points resulting in exceptionally high electrical conductivity even at room temperature [12].

Graphene is also known for its remarkable mechanical properties, ensured by the stability and strength of the  $\sigma$  bonds. Atomic force microscopy nanoindentation measurements have shown that a defect-free graphene sheet of effective thickness of 0.335 nm has an intrinsic strength of  $42 \text{ N m}^{-1}$ , which corresponds to a Young's modulus of  $E=1.0 \text{ TPa}$  and makes it one of the strongest materials known [13]. However, its strength deteriorates in presence of defects such as grain boundaries [14], functional groups [15] or vacancies [16]. Furthermore, while the interior of a graphene sheet is relatively chemically inert, a break of the  $\sigma$  bonds at the edges leads to a formation of dangling bonds which are highly reactive. Therefore, energy reduction can be achieved through edge termination with functional groups which consequently can alter the electronic structure of a material by opening a band gap and introducing different doping levels [17].

A combination of exceptional physico-chemical properties of graphene make it an interesting material for implementation in a variety of fields. Due to graphene's high charge carrier

mobility, superior thermal conductivity (2600 - 5300 W/(mK) at room temperature [18]) and strength, it could find applications in flexible electronics [19] and fast, low-power transistors [20]. It can also be applied in production of electrodes, the active and the interfacial parts for organic photovoltaic cells [21]. Furthermore, high electric conductivity and a very high surface-to-volume ratio makes graphene employable in energy storage devices as both active and passive material, by hosting ions in metal-ion batteries, storing electrostatic charges or acting as a conductive agent [22]. It was also found to be an advantageous material in electrochemical and biosensing applications, exhibiting higher sensitivity to the changes in local environment conditions than carbon nanotubes or silicon nanowires [23]. Graphene and its derivatives such as (reduced) graphene oxide can also be integrated into textiles making them electrically and thermally conductive, hydrophobic and UV-protecting [24].

### 1.3 Synthesis of graphene

Application of graphene in both industry and fundamental research is highly dependent on the quality of the material. Therefore, a substantial part of graphene-related studies is focused on the development of graphene production techniques in order to achieve atomic-scale control of the film quality and ensure a high level of reproducibility. Generally, graphene films can be synthesised by bottom-up and top-down approaches, i.e. grown from carbonaceous species on suitable substrates or produced from graphite or its derivatives by a variety of exfoliation methods. The most common methods and their associated advantages and limitations are briefly described in this section.

#### 1.3.1 Exfoliation techniques

Exfoliation of graphene from bulk graphite can be achieved through mechanical, chemical and thermal methods which break the van der Waals bonds that hold together adjacent graphene sheets in the parent material, graphite. The first free-standing graphene film was produced by micromechanical cleavage of Highly Ordered Pyrolytic Graphite (HOPG) using Scotch tape [3], as shown in Fig. 1.4(a). The method employs a normal force which is exerted on a bulk graphite surface a number of times until a single layer graphene sheet is isolated. While graphene flakes prepared by micromechanical cleavage are of high quality and relatively large size, the method itself is inefficient and arduous. Consequently, alternative methods have been developed which make use of self-lubricating properties of graphite and employ shear force to separate graphene sheets [25].

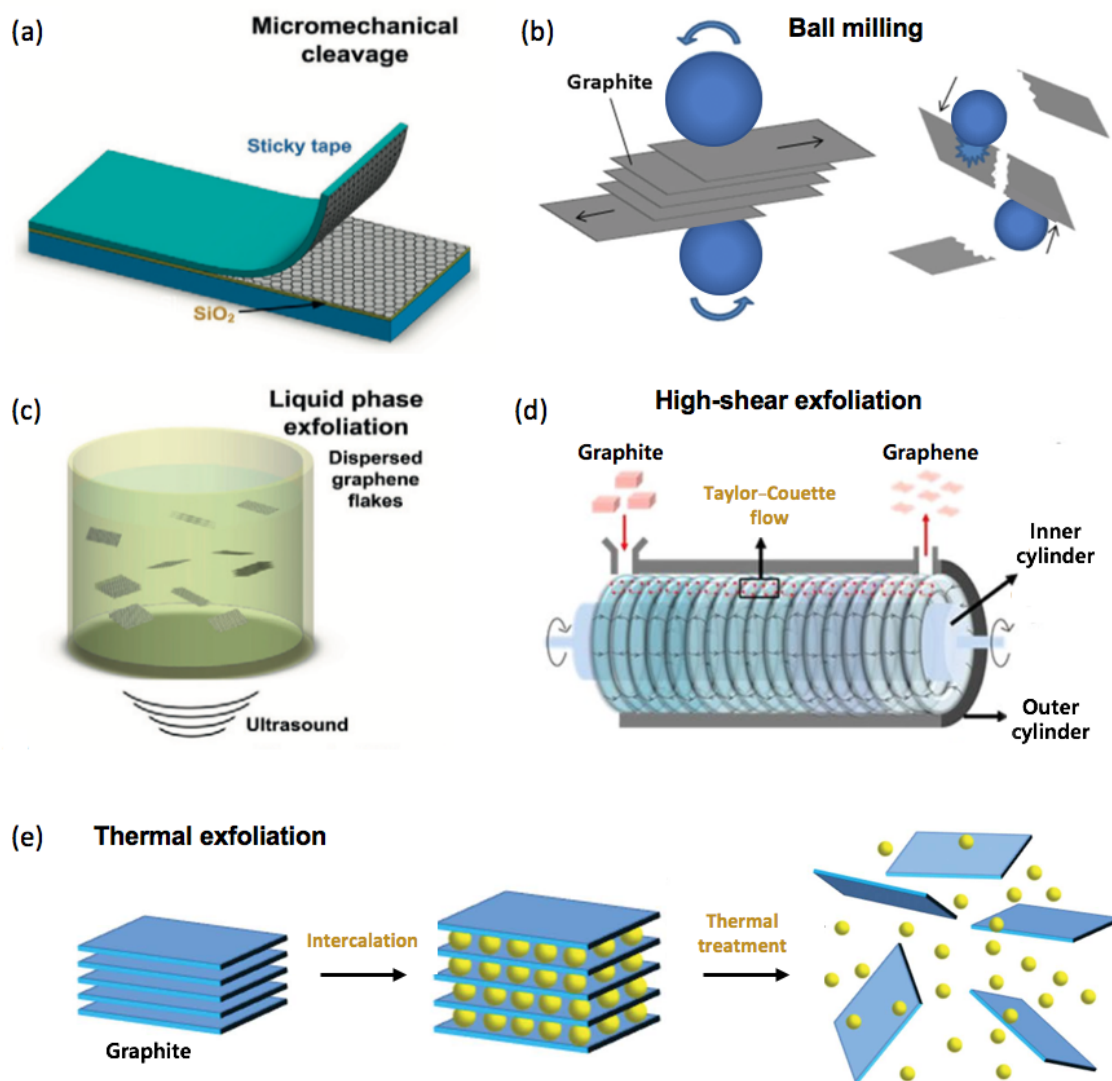


Figure 1.4: Top-down methods for graphene production. Images adapted from [26–29].

One of the most widely used approaches exploiting both normal and shear forces is liquid phase exfoliation (LPE), depicted in Fig. 1.4(c). In the LPE process, graphite is dispersed in a solvent, which is further sonicated in order to induce cavitation, i.e. formation of air bubbles due to pressure fluctuations [26]. The collapse of these bubbles generates shock waves, which result in propagation of lateral and normal compressive stress in graphite, leading to exfoliation of graphene layers [25]. The resulting suspension is ultracentrifuged to separate exfoliated flakes from unexfoliated material [26]. In addition to sonication, graphene sheets can also be isolated by high shear exfoliation, which is based on a Taylor-Couette flow. As shown in Fig. 1.4(d), graphite solution is confined between two concentric cylinders, inner of which is rotated at a speed that generates counter-rotating toroidal vortices [30]. The turbulence associated with rotation of the vortices serves as a source of shear force which exfoliates graphite in the solution [30]. Overall, LPE is fairly straightforward, scalable and produces flakes up to a few microns in size; however, most solvents and surfactants that deliver high yields of monolayer graphene and minimise their defect density are toxic and difficult to remove after exfoliation [26].

Graphite can also be produced using a ball milling technique, illustrated in Fig. 1.4(b). Here, graphite powder is placed into a medium containing grinding balls, made for instance from  $\text{ZrO}_2$ , and either stirred or rotated together with the enclosing tank [25]. The interaction between grinding balls and bulk graphite generates a shear force, which weakens van der Waals bonds and results in graphene platelet exfoliation [31]. Ball milling can be wet or dry depending on whether graphite is dispersed in a solvent or chemically-inert inorganic salts, which are washed off at the end of the process [25]. The method can be easily scaled to produce graphene platelets of good quality, but their lateral size is small, typically reaching up to  $1 \mu\text{m}$  [32] due to fragmentation caused by high-speed normal collisions between grinding balls and bulk graphite [33].

Graphene can also be exfoliated by thermal treatment of intercalated graphite or graphite oxide (Fig. 1.4(e)). The method is based on thermal decomposition of functional groups attached to adjacent graphite layers [34]. The by-products of decomposition reactions exert pressure on graphite layers, which breaks van der Waals bonds and separates graphene sheets from the bulk. The process is quick, lasting from a few seconds to a few minutes, and occurs at temperatures between  $200 \text{ }^\circ\text{C}$  and  $1050 \text{ }^\circ\text{C}$  [35]; however, the graphene flakes produced are often found to be structurally and topologically defective [35].

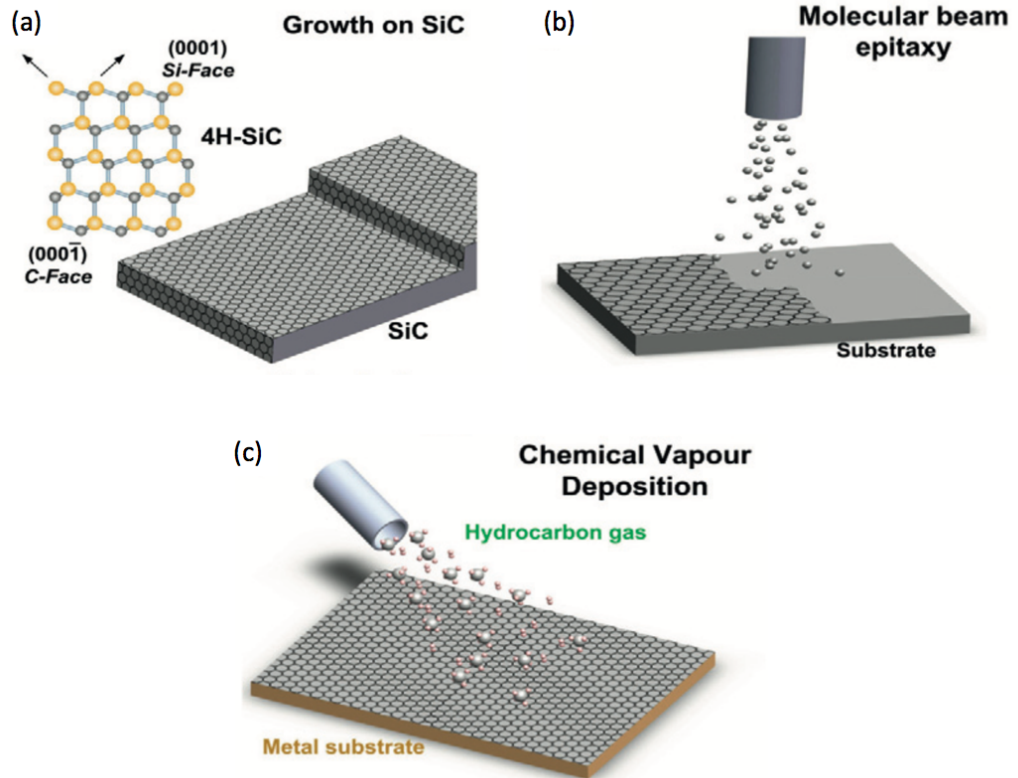


Figure 1.5: Bottom-up methods for graphene production. Images adapted from [26].

### 1.3.2 "Bottom-up" growth

Alternatively to the top-down approaches discussed previously, graphene can be grown epitaxially on crystalline substrates from carbonaceous species provided either by an external source or by the substrate itself. A common approach for epitaxial growth of graphene is based on silicon sublimation from hexagonal SiC wafers, illustrated in Fig. 1.5(a). Here, the Si-terminated (0001) surface of SiC is annealed in Ar atmosphere at temperatures typically ranging from 1500 °C to 2000 °C [36]. The Ar atmosphere controls the silicon sublimation rate and allows higher process temperature, which consequently improves surface diffusion and reconstruction of underlying carbon atoms into a graphene-like film [26]. The resulting carbon-terminated surface stays partially bonded to Si through covalent bonds, which can be broken by hydrogen intercalation. The domains of graphene grown on SiC are of high quality, with size reaching up to  $\sim 50 \mu\text{m}$ ; however, the production is not easily scalable due to a high price of SiC wafers and energy-intensive nature of the process [26].

Graphene films can also be grown by molecular beam epitaxy (MBE), which is a technique widely used in semiconductor growth [26] (Fig. 1.5(b)). The process relies on carbon sub-

limation from a heated graphite filament source in the form of carbon cluster beams which impinge on a substrate surface and deposit the carbon necessary for the film growth [26]. MBE is typically carried out in ultrahigh vacuum on a variety of substrates like sapphire, SiC, Si, and Ni [37], and at temperatures ranging between 300-1850 °C [38, 39]. Due to the lack of control of the deposition process, the resulting graphene flakes greatly vary in size, are defective and have a multilayer structure [26]. Their quality is also heavily affected by the substrate surface morphology which can be improved by surface preparation methods such as high-temperature annealing.

Another very widely applied technique for graphene growth is chemical vapour deposition (CVD), pictured in Fig. 1.5(c). In this approach, a substrate is exposed to carbonaceous precursors, which are adsorbed on the substrate surface as a way to minimise energy. The process is followed by formation of nuclei, surface chemical reactions and lateral growth of graphene islands until they merge with neighbouring domains [40]. A number of different substrates can be used for graphene growth by CVD, most common of which are transition metals (Cu, Ni, Pt, Co) known for their catalytic properties [41]. A variety of precursors in solid, liquid or gaseous forms can be used as well, with hydrocarbons being prevalent species [41]. The quality, nucleation density and size of grown islands is highly dependent on experimental conditions of the CVD process such as pressure, temperature or the amount of carbon solubility in a chosen substrate. Normally, the growth strategies aim to reduce graphene nucleation density in order to maximise the island size and reduce the number of rotational grain boundaries that impair the electrical and mechanical properties of the resulting film. Nonetheless, CVD is a suitable method for mass production of high quality graphene domains of size potentially reaching of the order of a millimetre [40], [42]. This method is used to produce samples for the analysis presented in this thesis and it is described in greater depth in Section 2.3.

## 1.4 Kinetics of graphene growth by CVD

Graphene applications in industry demand scalable and controllable production of large, high-quality films. CVD provides a reproducible way to grow graphene islands of desirable properties, but successful application of the method relies on in-depth understanding of graphene growth kinetics. Every step of the CVD process, from the introduction of a precursor into a reaction chamber to aggregation of carbon species and subsequent growth of graphene islands, is highly affected by a number of growth parameters such as chemical composition of a

precursor, its decomposition pathways [43] and partial pressure [44], the composition of auxiliary gases [45], overall reaction pressure [46] and temperature [47]. The growth mechanisms are also heavily influenced by substrate qualities like surface roughness [48], purity [49], crystalline orientation and amount of carbon solubility [50]. The intricate details of the processes taking place on the surface of a substrate are usually not well-known, but careful optimisation of the growth conditions and macroscopic modelling of the growth kinetics enable the control of island morphology, their nucleation density, size, growth rate, as well as number of layers and their stacking order.

A few attempts have been made to describe isothermal phase transformation processes during graphene growth by CVD, one of which is proposed by Kim *et al.*, who employ a Johnson-Mehl-Avrami-Kolmogorov (JMAK) model to characterise graphene formation on catalytic substrates [51]. The JMAK theory generally describes sigmoidal phase transformations developing via nucleation, growth and impingement, and relies on three major assumptions: infinite size of a system, random homogeneous nucleation and termination of particle growth upon mutual contact [52]. It also divides the nucleation mechanisms into two types: a constant nucleation rate (CNR) mechanism, which refers to nucleation taking place at a constant rate over the entire transformation period, and site-saturated nucleation (SSN), which describes nucleation happening only at the beginning of the transformation before the growth process [53]. The JMAK model is known for its simplicity and has been widely applied to study a variety of transformations in solid state materials, including polarization reversal in ferroelectric films [54] and polymer crystallization [55]; however, its applicability in the growth of thin films has been debated due to the finite nature of substrates and occasionally observed heterogeneous nucleation [52]. Nonetheless, Kim *et al.* presented a modified JMAK model based on site-saturated nucleation of graphene, island growth and coalescence until a saturated area coverage,  $A_{\text{sat}}$ , is reached [51].

The group produced graphene samples by CVD on Cu substrates using methane ( $\text{CH}_4$ ) as a precursor [51]. The growth process was described in terms of a carbon crystallisation mechanism which is initiated by the adsorption and dissociation of  $\text{CH}_4$  on the Cu surface, leading to a production of active carbon monomers [51], as illustrated in Fig. 1.6(a). The nucleation of stable supercritical graphene domains occurs when the concentration of active carbon species,  $c_{cu}$ , reaches a critical supersaturation level,  $c_{nuc}$  [51]. As the domains grow via attachment of nearby carbon species (assumed to be carbon monomers),  $c_{cu}$  starts dropping and no further substantial nucleation takes place [51]. Finally, the growth of the supercritical nuclei ceases when  $c_{cu}$  reaches the equilibrium level between attachment and desorption of

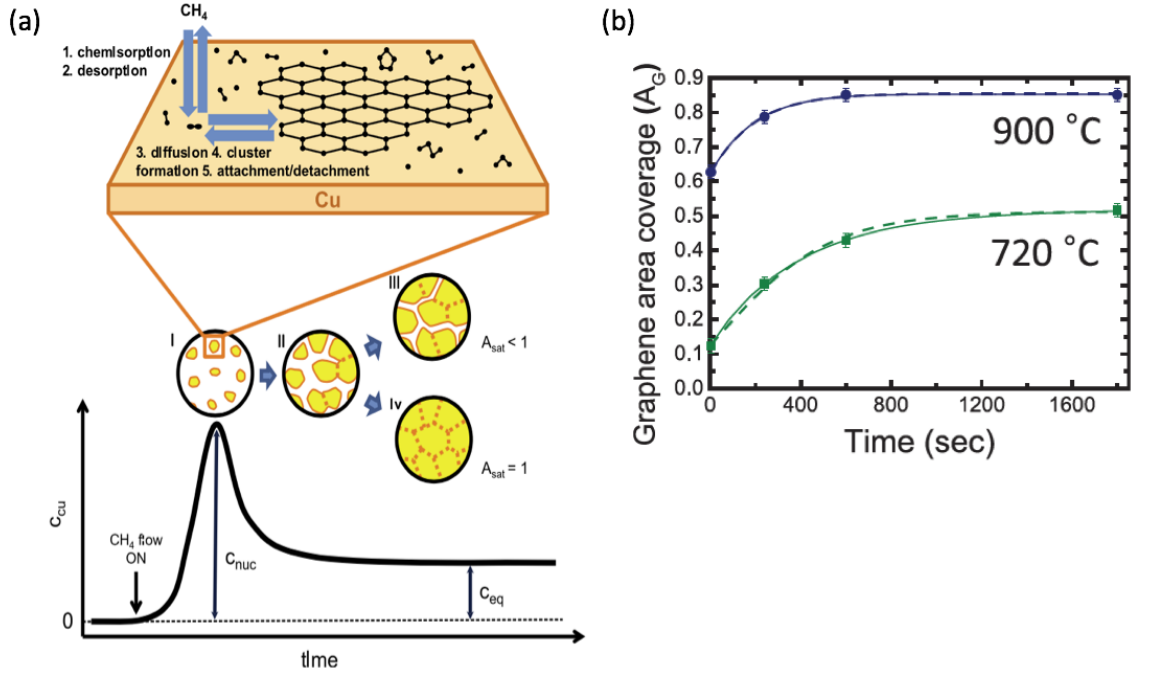


Figure 1.6: Site-saturate graphene growth model (a) and a modified JMAK equation fitting to the graphene growth data obtained by Kim *et al.* [51].

active carbon species,  $c_{eq}$  [51]. Depending on the supersaturation level,  $(c_{nuc} - c_{eq})$ , graphene domains stop growing to reach incomplete substrate coverage ( $A_{sat} < 1$ ) or grow until they merge and form a continuous film ( $A_{sat} = 1$ ) [51]. Furthermore, it is assumed that dissociation of CH<sub>4</sub> stops after nucleation, and graphene grows only at the expense of the carbon surface concentration above the equilibrium level [51]. The resulting growth data (Fig. 1.6(b)) was fitted with a modified JMAK equation

$$A_G = A_{sat}(1 - \exp(k(t - t_0)^n)), \quad (1.4.1)$$

where  $A_G$  is the fraction of substrate area covered by graphene,  $k$  is the reaction rate constant,  $t_0$  is nucleation time and  $n$  is the Avrami exponent, which is related to the dimensionality of the system [51].

Nevertheless, the JMAK model has been criticised due to a number of debatable and unphysical assumptions being made to describe graphene growth by CVD. Even though not much is known about the precise composition of film-forming species on Cu surface, DFT calculations show that the assumed surface supersaturation with carbon monomers is highly unlikely due to high energy barriers associated with complete CH<sub>4</sub> dehydrogenation [56]. Instead, it is expected that the most abundant carbon species on Cu should be CH and CH<sub>3</sub> [56]. Moreover,

it would be false to assume that adsorption of the precursor would stop after nucleation in gas-phase CVD.

Due to the inaccuracies associated with the application of the JMAK model, Celebi *et al.* have suggested to model graphene growth via a modified Gompertz function [57]. Gompertzian kinetics typically describes processes that evolve in a sigmoidal manner, i.e. consist of three growth phases corresponding to different growth rates (slow-fast-slow), and have an associated lag parameter defining the growth rate acceleration time to its maximal value [58]. Originally, Gompertz curve was used to describe human mortality [59] and later was adopted (with modifications) by biologists and economists to model a variety of processes such as algae [60], tumor growth [61], chemical neurotransmission currents [62] and income distribution [63].

Celebi *et al.* modelled graphene growth from a perspective of Gompertzian kinetics involving a number of assumptions contradicting the rationale behind the JMAK model. According to them, the general growth mechanism of graphene begins with adsorption, catalytic decomposition and dehydrogenation of a precursor (the group used ethylene) on the surface of Cu [57]. The active carbon species are thought to be a mixture of carbon monomers, dimers and intermediate species which diffuse and either nucleate when their concentration reaches a critical supersaturation level or desorb [57]. The subsequent island growth proceeds via attachment of carbon reactants at an initially growing rate, which indicates that the main carbon source for the growth is provided by a continual supply of a precursor [57], as opposed to the initial supersaturation level. Furthermore, Celebi *et al.* claim that carbon species may diffuse under the existing graphene flakes causing secondary nucleation and therefore secondary layer growth, which terminates when the primary layer reaches full coverage [57]. Depending on the amount of available precursor, graphene islands grow to reach either partial or complete/saturated substrate coverage. The overall growth process is defined by a modified Gompertz equation

$$A_t = A_{max} \exp \left( - \exp \left( - \frac{\mu_m e}{A_{max}} (t - \lambda) + 1 \right) \right), \quad (1.4.2)$$

where  $A$  corresponds to the graphene island area,  $A_{max}$  is the maximum flake area at the saturation phase,  $e$  is Euler's number,  $\mu_m$  is the maximum growth rate,  $t$  is time and  $\lambda$  is the time lag. The fit of the function to the data is presented in Fig. 1.7.

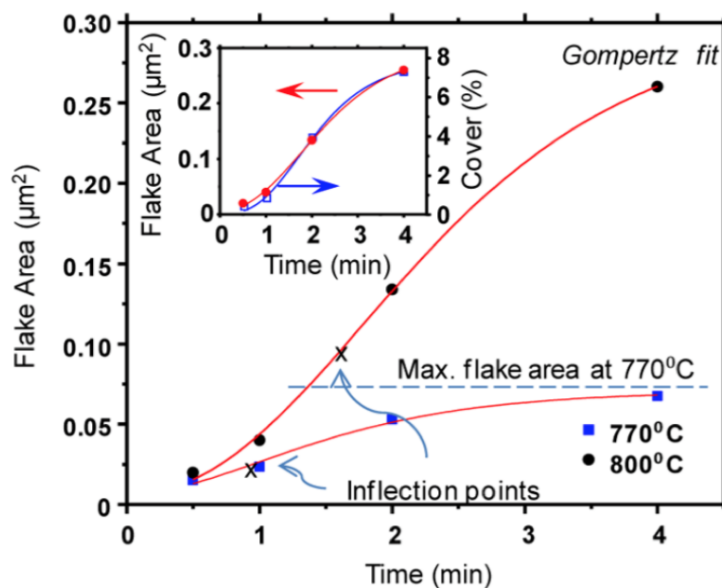


Figure 1.7: A modified Gompertz equation fitting to the graphene growth data obtained by Celebi *et al.* [57].

## 1.5 Organisation of thesis

This thesis is organised as follows: the theoretical background of the experimental techniques used to grow and characterise graphene samples are presented in Chapter 2; experimental instrumentation and a sample preparation procedure is discussed in Chapter 3; Chapter 4 covers the analysis of graphene growth kinetics and the impact of substrate texture on the island growth. Finally, Chapter 5 summarises the results and outlines a few suggestions for further work.

## 1.6 Summary

This chapter overviewed the structure and physico-chemical properties of monolayer graphene. "Top-down" and "bottom-up" graphene production methods were summarised, outlining their impact on the structural properties of graphene samples. Two kinetic graphene growth models - modified JMAK and modified Gompertz - were introduced.

## Chapter 2

# Experimental techniques

This chapter overviews the experimental techniques used to grow and characterise graphene samples for the graphene growth study presented in this thesis. The theoretical background of each technique is discussed followed by a review of how it is applied in graphene research.

### 2.1 Raman scattering

#### 2.1.1 Introduction

The discovery of Raman scattering dates back to 1928, when the Indian physicist C. V. Raman observed that a spectrum of the light scattered by the molecules in a dust-free liquid contained frequencies that were not present in the spectrum of the incident light [64]. This phenomenon, originating from characteristic vibrational frequencies of molecules, earned Raman the Nobel Prize in 1930.

For a few decades, the development of experimental methods for Raman spectroscopy remained slow, with a mercury arc being the only suitable, yet not a perfect source of radiation. Due to the weakness of Raman scattering, the intensity of which can be as low as  $10^{-5}$ - $10^{-6}$  of the intensity of the incident light [65, 66], samples had to be relatively large and of high quality; otherwise, fluorescence from impurities and scattering from crystal defects could overpower Raman scattering [65]. However, the situation changed greatly with the introduction of lasers. Highly monochromatic beams of frequencies ranging over the whole visible spectrum and an increase in power per unit area attainable at the sample facilitated the study of both ordinary and resonance Raman scattering of even very small samples (approx.  $10^{-12}$  cm<sup>3</sup> for solids).

Nowadays, Raman spectroscopy serves as a powerful technique to study vibrational, rotational and electronic transitions of molecules and materials at a broad range of pressures and temperatures [66,67]. It requires little to no sample preparation, is non-destructive, and offers fast and simple sampling with high spectral resolution [68,69]. As a result, spectra can be obtained from a wide range of samples: crystals, powders, liquids, gases, etc.

### 2.1.2 Origin of Raman scattering

Non-resonant Raman scattering is an inelastic scattering process arising from an interaction between a molecule or solid and a photon with an energy that is lower than the difference between the ground and the first excited state [66]. During this interaction, an electron absorbs a photon of the incident electromagnetic radiation and gets promoted from a vibrational level of the ground electronic state to a virtual (non-stationary) state, which has a very short lifetime ( $\approx 10^{-14}$  s) defined by the Uncertainty Principle. As opposed to elastic scattering, also known as Rayleigh scattering, in which the system returns to the initial state by an emission of a photon of the same energy as the one absorbed, Raman scattering results in an emission of either a lower or higher energy photon and a change in a vibrational state of the system [65]. The relative intensities of Rayleigh and Raman scattering depend on the direction of observation relative to the direction of irradiation, the chemical composition and the physical state of the target; however, the intensity of Raman scattered light reaches approximately  $10^{-2}$ - $10^{-3}$  of the intensity of Rayleigh scattered light [65,66].

The application of laser sources made simple observations of another scattering effect - the resonance Raman (RR) effect - feasible. RR scattering is observed when the energy of the incident photon is high enough to trigger an electronic transition in the sample [66]. The resonance condition enhances the intensity of Raman scattering by a factor of  $10^3$  to  $10^5$  making it a suitable technique to identify vibrations of interest above a complex background [68,69].

The Raman effect can be further divided into two types: Stokes and anti-Stokes scattering. In Stokes scattering, an electron decays to an energetically higher vibrational level than the one it was promoted from. Consequently, the excess energy is emitted in a form of a photon that has a lower frequency than the incident photon. In the anti-Stokes scattering, an electron decays to an energetically lower vibrational state leading to a creation of a photon of a higher than incident frequency [65]. The energy level diagrams for the ordinary Stokes, anti-Stokes and Rayleigh scattering are presented in Fig. 2.1, while the comparison of the

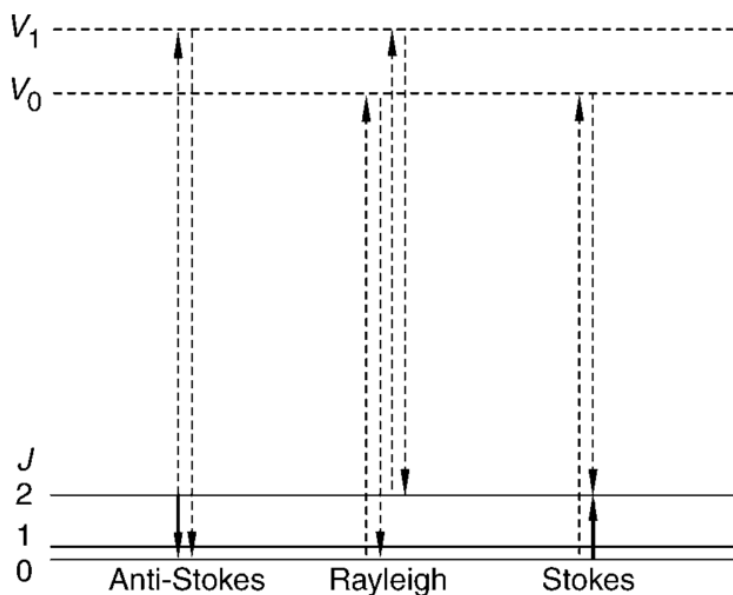


Figure 2.1: Rayleigh, Stokes and anti-Stokes scattering mechanisms involving real states  $J=0, 2$  and virtual states  $V_0$  and  $V_1$  [67].

energy level diagrams for the resonant and non-resonant Stokes scattering is presented in Fig. 2.2. Under normal conditions, the intensity of the anti-Stokes scattering is substantially lower than the Stokes scattering with the difference arising from an exponential decrease of the thermal population of higher energy states; therefore, the ratio of these intensities can give an indication of the temperature of a sample.

A Raman spectrum is typically described in terms of the Raman shift, i.e. the magnitude of the wavenumber shift from the incident wavenumber [65]. A complete Stokes spectrum covers the shift for almost all rotational and vibrational levels, and lies in the visible region of the spectrum for 400-600 nm incident radiation. Therefore, only one detector and one dispersing system are needed to study most of rotational and vibrational transitions of molecules.

### 2.1.3 Complementarity of Raman and infrared spectra

Raman spectroscopy together with infrared (IR) absorption spectroscopy can provide almost full information about the frequency, amplitude and number of vibrations of a molecule in the ground electronic state [66]. Due to different interaction mechanisms between a photon and a target, both spectra result from different selection rules which determine whether a certain vibration is Raman and/or IR active.

To explain Raman and IR activity from the quantum mechanical perspective, one needs to

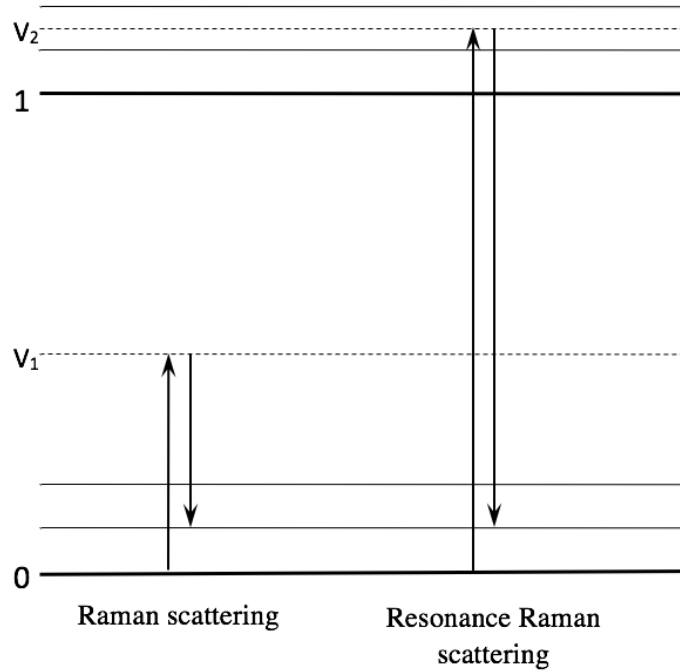


Figure 2.2: Non-resonant and resonant Raman (Stokes) scattering mechanisms involving ground electronic states and virtual states  $V_1$  and  $V_2$ .

model the vibrations of a system (e.g. molecule or solid) in terms of an anharmonic oscillator which, upon an interaction with a photon, passes from an energy state  $m$  to an energy state  $n$  if the transition probability is higher than zero. A Raman-active vibration originates from a change in polarisability caused by an interaction with the incident photon, and its transition probability is proportional to the square of the absolute value of the transition moment defined by the equation:

$$|(\alpha_{ij})_{nm}| = \int_{-\infty}^{\infty} \Psi_n^* \alpha_{ij} \Psi_m d\tau \quad (2.1.1)$$

where  $\Psi_m$  and  $\Psi_n^*$  are the wavefunctions of the initial and final vibrational states involved in the transition, the transition operator is the polarisability tensor component of the molecule or solid,  $\alpha_{ij}$ , and integration is carried out over the volume element  $d\tau$ . If there is any change of polarisability over the volume of the molecule or a unit cell of the solid, the transition moment is non-zero and the transition is active in the Raman spectrum.

An IR-active vibration is caused by a change in the dipole moment upon the interaction, and its transition moment is given by the equation:

$$|M_{nm}| = \int_{-\infty}^{\infty} \Psi_n^* \boldsymbol{\mu} \Psi_m dQ \quad (2.1.2)$$

where the dipole moment,  $\mu$ , is the transition operator, and the transition is active in the IR spectrum if there is non-zero change in the dipole moment over the normal coordinate of vibration,  $Q$  [68].

For molecules that have a centre of symmetry, Raman and IR-active vibrations satisfy the principle of mutual exclusion, which states that a vibration active in one spectrum will be absent from the other. For molecules without a centre of symmetry, vibrations will be active in both spectra; however, they will have different intensities [66, 68].

#### 2.1.4 Raman spectrum of graphene

Raman spectroscopy is one of the most common techniques used for graphene characterisation. A reasonably strong signal can be detected while investigating even a single layer of atoms due to the resonant properties of the Raman scattering mechanism [70]. This method can give information about the number of graphene layers, their stacking order, grain boundaries and edge structure of graphene crystals, chemical impurities and various other properties of the sample [71, 72]. In this thesis, Raman spectroscopy is used to examine the thickness of graphene islands and their level of disorder.

Figure 2.3 shows a typical Raman spectrum of graphene which contains three prominent peaks:  $D$ ,  $G$  and  $2D$  (sometimes referred to as  $G'$ ). In order to interpret the origin of these peaks, it is necessary to look at the phonon dispersion in graphene. As mentioned before, Raman scattering leads to changes in vibrational states of molecules, which collectively form phonons in one or more dimensional materials. Monolayer graphene has two carbon atoms per unit cell, motion of which gives rise to six phonon bands. In-phase and out-of-phase vibrations of the two atoms correspond to the acoustic (A) and optic (O) phonon branches respectively, each of which has one out-of-plane (o) and two in-plane (i) vibrational modes. While in the out-of-plane mode the atoms oscillate in the transverse direction to the graphene plane, in the in-plane mode the atoms can vibrate either parallel to the carbon-carbon bond generating longitudinal (L) modes or perpendicularly to the carbon-carbon bond generating transverse (T) modes. Hence, along the high-symmetry lines between the  $\Gamma$ , M and K points of the graphene Brillouin zone in reciprocal space, the six phonon modes, namely oTA, iTA, iLA, oTO, iTO and iLO, give rise to the phonon dispersion curves depicted in Figure 2.4.

The  $G$  band at about  $1580 \text{ cm}^{-1}$  is associated with carbon-carbon bond stretching and occurs due to the first order Raman scattering off a doubly degenerate in-plane optic phonon mode at the Brillouin zone centre,  $\Gamma$ . However, the scattering mechanisms giving rise to the  $D$

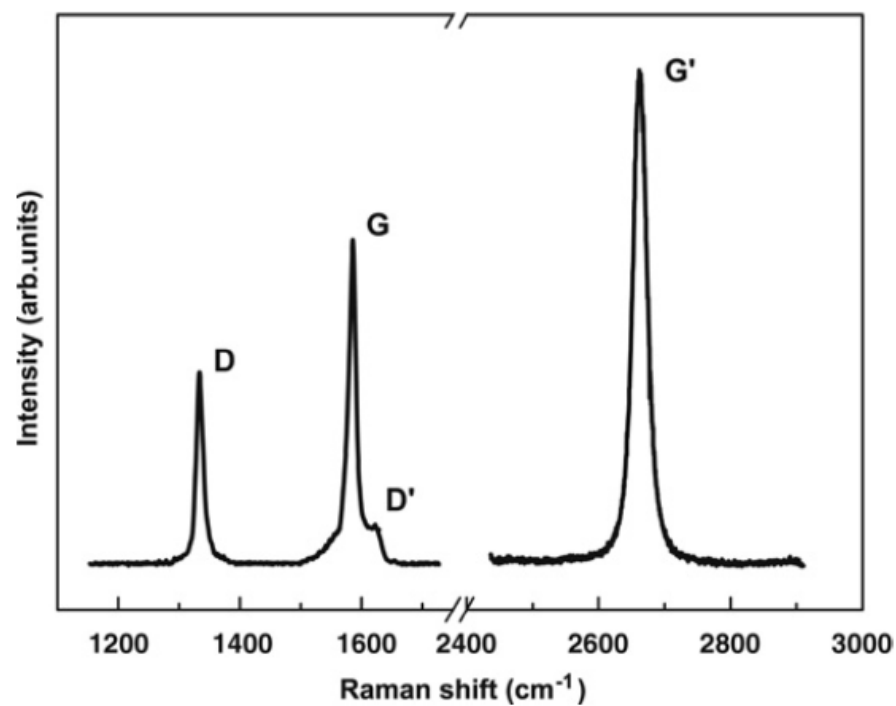


Figure 2.3: Raman spectrum of graphene taken with a 2.41 eV laser excitation energy [71].

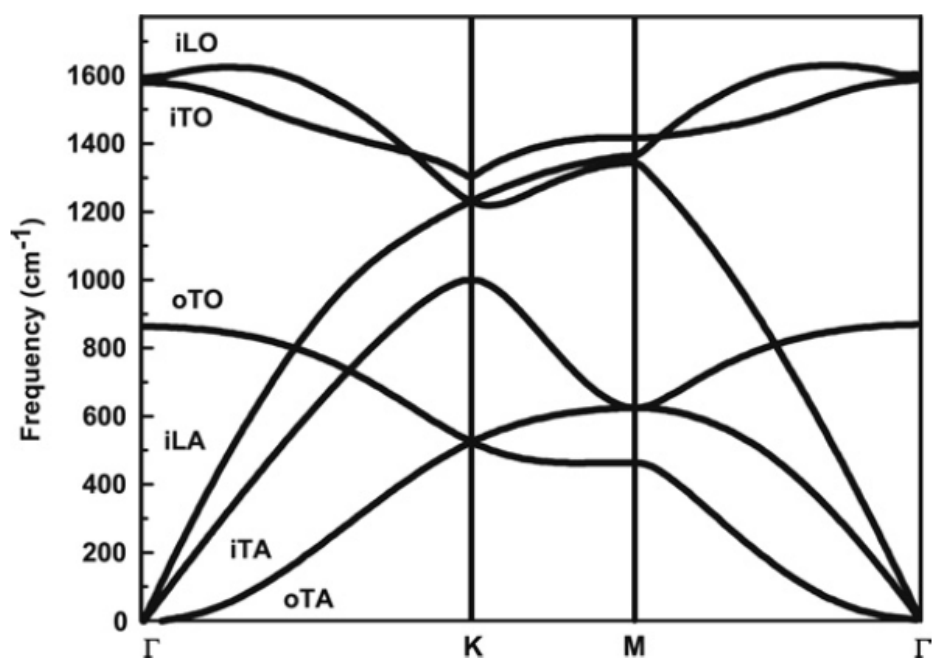


Figure 2.4: Phonon dispersion relation of monolayer graphene arising from iLO, iTO, oTO, iLA, iTA and oTA vibrational modes [71].

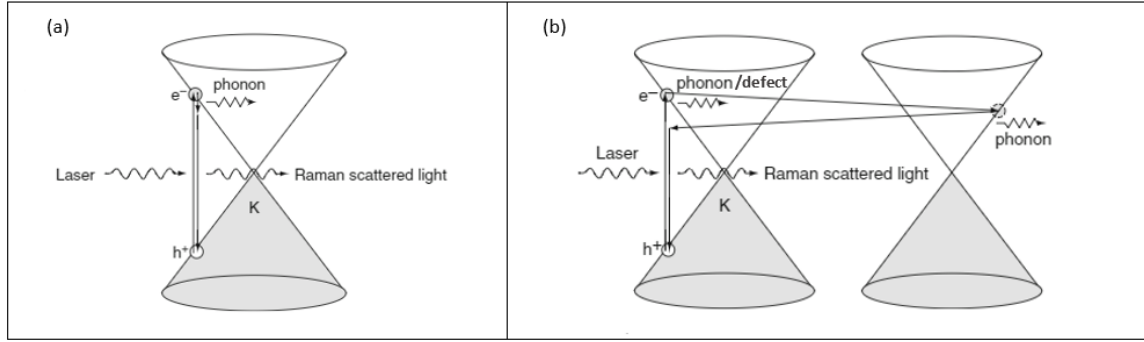


Figure 2.5: Resonant Raman scattering process generating  $G$  band (a) and doubly resonant Raman scattering process generating  $2D$  and  $D$  bands [70].

and  $2D$  bands are second-order processes. In the case of the  $2D$  band, an electron near a  $K$  point is inelastically scattered by an iTO phonon to a nearby  $K'$  point. Then, the electron is scattered back to its previous state by a phonon of the same momentum, which is followed by a recombination of the electron and a hole along with the emission of a photon. A similar doubly resonant process involving  $K$  and  $K'$  points generates the  $D$  band; however, here, an electron is first elastically scattered by a defect of a crystal such as a vacancy site or an edge, and then it is inelastically scattered back by an iTO phonon. The first and the second order scattering processes are depicted in Figure 2.5. The Raman shift of the  $D$  and  $2D$  bands shows a dispersive behaviour which depends on the energy of the laser. For a laser energy of 2.41 eV, the  $D$  and  $2D$  bands are approximately at  $1350\text{ cm}^{-1}$  and  $2700\text{ cm}^{-1}$  respectively [70, 71].

The relative intensities of the  $G$ ,  $D$  and  $2D$  peaks can be used to deduce certain qualities of a graphene sample. For instance, for a number of graphene samples examined using a laser of a fixed energy, the ratio of the  $D$  and  $G$  peaks correlates with the defect density in the sample, with  $D$  band being very weak or absent in a spectrum of pristine graphene [70]. Also, the relative intensities of the  $2D$  and  $G$  bands can give information about the thickness of graphene. For a monolayer graphene, the intensity of the  $2D$  band is large in comparison to the  $G$  band, and can be explained in terms of an additional hole scattering process that increases the intensity of the  $2D$  band. Furthermore, the number of Lorentzians that can be fitted to the  $2D$  band and their full width at half maximum (FWHM) can serve as an indicator of the number of graphene layers present and their stacking order [71].

## 2.2 Scanning electron microscopy

### 2.2.1 Introduction

The theoretical basis for a microscopy technique that employs an electron beam instead of visible-light photons to probe a specimen was laid in 1920s by Busch and de Broglie [73]. It relied upon two central ideas: the discovery made by Busch that axially symmetric electric and magnetic fields could act as lenses for charged particles, and de Broglie's hypothesis, i.e. a proposition that all matter had wave-like properties [73]. The first true scanning electron microscope (SEM) was developed in 1942 and attained 50 nm resolution. It was outperformed by transmission electron microscopes, which reached higher resolution for thin samples; however, it was soon noticed that SEMs could reveal three-dimensional information about the surface of a bulk specimen over a wide range of length-scales [73].

Nowadays, the SEM serves as a powerful tool to analyse the chemical composition, microstructural, electric and magnetic properties of a wide range of both physical and biological specimens [74]. Modern microscopes reach sub-nanometer resolution, have a large depth of field and fast micrograph acquisition time. The specimen size is limited by the dimensions of the specimen stage, and, while certain specimens such as bioorganic nanomaterials require complicated sample preparation procedures, most nanomaterials like nanowires or carbon nanotubes can be examined without any preparation [74, 75].

### 2.2.2 Electron-specimen interactions

In SEM, a focused electron beam is scanned across the specimen surface, and an image is formed from the signals produced by both elastic and inelastic interactions between the electron beam and the atoms of the specimen [74, 75].

Elastic scattering can occur between an incident electron and either atomic nuclei or outer shell electrons of the specimen with negligible energy loss. A single elastic scattering event can result in a change in direction of the primary electrons by more than  $90^\circ$ ; therefore, a series of such events will often lead to electrons travelling back to the surface of the specimen and escaping [74], a process known as electron backscattering.

Inelastic scattering results from collisions between the primary electrons and the specimen's atomic nuclei and electrons with a substantial energy transfer to the atom. Collisions with loosely bound outer electrons lead to ejection of secondary electrons and ionisation. Inelastic

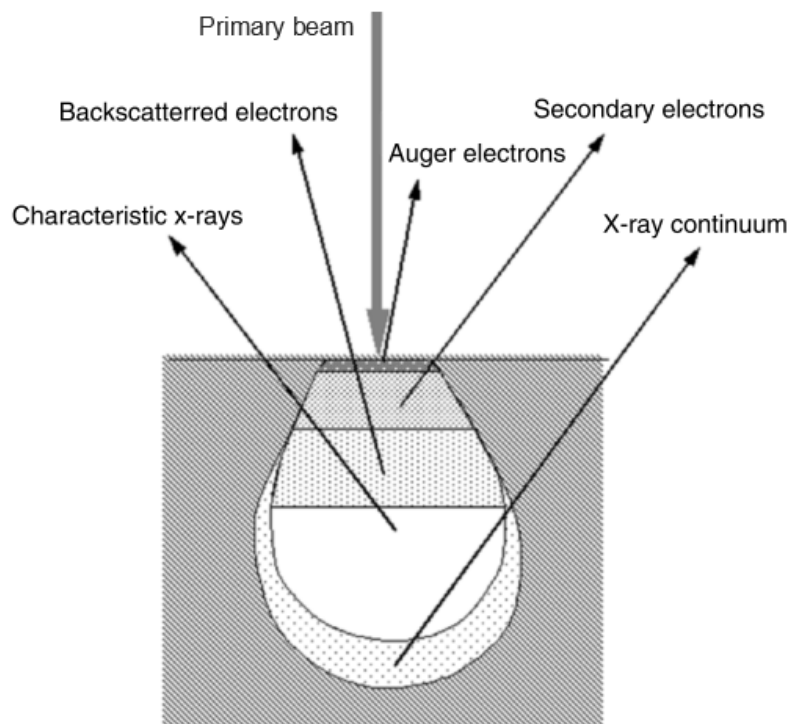


Figure 2.6: A schematic of signals produced by scattering events between an incident electron beam and a specimen [75].

scattering can also generate Auger electrons, characteristic x-rays and cathodoluminescence; however, only secondary and backscattered electrons, which will be described further in more detail, are used in this thesis to characterise graphene samples.

The depth and volume of the specimen that is penetrated by the electron beam is directly proportional to the energy of the beam and inversely proportional to the density of the specimen. For samples of low atomic number, this region resembles the shape of a tear drop, while samples of higher atomic number tend to have a hemispherical interaction volume [75]. Fig. 2.6 shows a cross-section of a specimen and the signals produced by the electron beam-specimen interactions.

### 2.2.3 Imaging with secondary electrons

The secondary electrons are low-energy electrons ( $<50$  eV) arising from inelastic interactions between the incident electrons and atomic electrons of a sample. They are strongly absorbed by the specimen; therefore, only interactions originating in the region of a few nanometers from the surface can lead to a detectable signal [74, 75]. The yield, or number of secondary electrons ejected per primary electron, is approximately equal to or greater than 1; hence,

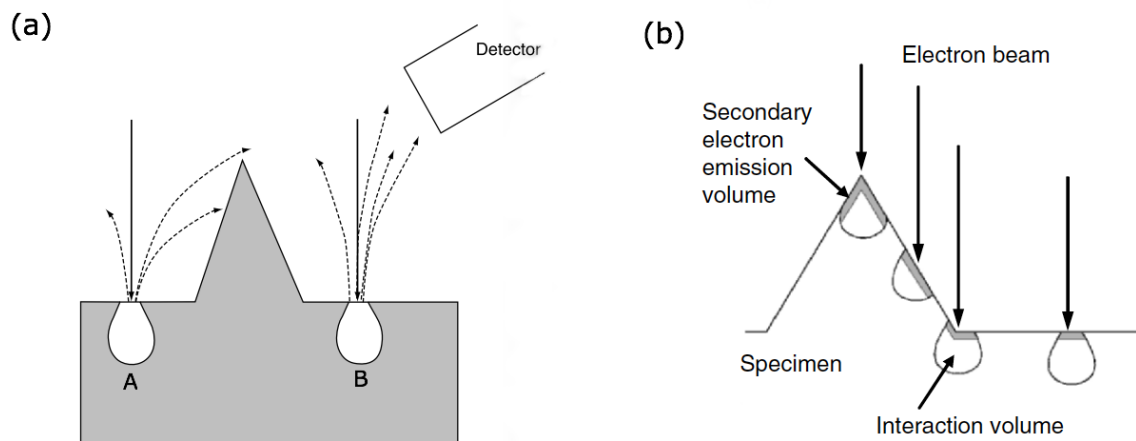


Figure 2.7: The contrast difference in SEM imaging originates from a varying signal strength due to prominences blocking a fraction of secondary electrons from reaching a detector (a) and a difference in intensity of the secondary electron emission due to the topography of a sample (b) [75].

they are often used as a primary imaging mechanism in SEM [76]. Due to a small interaction volume, secondary electrons typically resolve surface features down to lengthscales of the order of 10 nm.

SEM micrographs that are obtained using secondary electrons reveal the topography of the sample surface which is displayed in terms of a contrast difference that arises due to the variation of the interaction-induced signal. Fig. 2.7 (a) depicts a prominence on a sample surface and its influence on the detection of secondary electrons. A fraction of the electrons coming from the interaction region A is blocked from reaching the detector by the prominence, which results in a darker contrast as compared to the number of electrons and the contrast detected from the interaction region B. Furthermore, the local curvature of the specimen surface affects the shape of the interaction volume and hence the electron emission efficiency. In Fig. 2.7 (b) it can be seen that the secondary electron emission is most intensive at the tip of the prominence and it decreases at the parts of surface that are perpendicular to the electron beam, which results in higher and lower contrast respectively.

#### 2.2.4 Backscattered electrons and their diffraction

Topographic and compositional information about a sample can also be obtained using backscattered electrons (BSEs) [75]. These electrons undergo single or multiple scattering events and escape the surface of the specimen at energies higher than 50 eV and angles that are greater than  $90^\circ$  with respect to the impinging electron beam. The yield of the

BSEs is approximately 0.1-0.5 and is dependent on the elemental composition of a sample. Heavier elements with more positive charge in the nucleus produce a higher backscattering signal than the lighter ones, which gives rise to an atomic number contrast in SEM micrographs [75]. Due to the high energy of BSEs, which typically reaches 60-80% of the energy of the primary beam, and therefore a relatively large electron-specimen interaction volume, their lateral resolution is two orders of magnitude lower than the resolution of the secondary electrons; however, they can produce different topographical images that give information about the structure of the sample deeper beneath its surface [75].

BSEs can be used to perform electron backscatter diffraction (EBSD) - a quantitative technique used to examine crystallographic features of most inorganic crystalline materials. It can give information about the orientation of grains, their size and character of their boundaries. EBSD can also be used to determine the influence of grain boundary crystallography on mechanical, chemical and electrical properties of a specimen and determine the strain variations and fracture planes in a microstructure [75, 76]. In this thesis, EBSD is used to determine crystallographic orientation of copper grains under graphene islands to examine any growth differences arising due to varying substrate orientations.

As mentioned before, BSEs are deflected at high angles; therefore, the sample is normally placed at a  $20^\circ$  angle to an incident beam with a 10-30 kV accelerating voltage. The primary electrons first undergo inelastic and diffuse scattering which results in a number of electrons reaching every set of lattice planes at their corresponding Bragg angles,  $\Theta_B$ . Consequently, elastic scattering takes place. As electron diffraction occurs in all directions, the diffracted radiation propagates along the surface of a double cone, axis of which is normal to the reflecting atomic plane. At typical electron wavelengths and interplanar spacings of a lattice, the opening angle of the double cone is nearly  $180^\circ$ . Therefore, the cone is almost flat and, upon the intersection with the phosphor screen of an EBSD camera, forms a Kikuchi band which is enclosed by two parallel straight lines and has an angular width of  $2\Theta_B$  [77, 78]. A diagram of the process is presented in Fig. 2.8

A complete Kikuchi pattern of a crystal under the beam contains a set of Kikuchi bands of varying width which are attributed to distinct crystallographic planes. The intersection of several Kikuchi bands typically corresponds to a high-symmetry crystallographic orientation [78]. The produced pattern can be further measured by analysis software and compared with those predicted for a crystal structure. EBSD data can be obtained automatically, at fast indexing rates and with angular resolution of  $0.5-1.5^\circ$ .

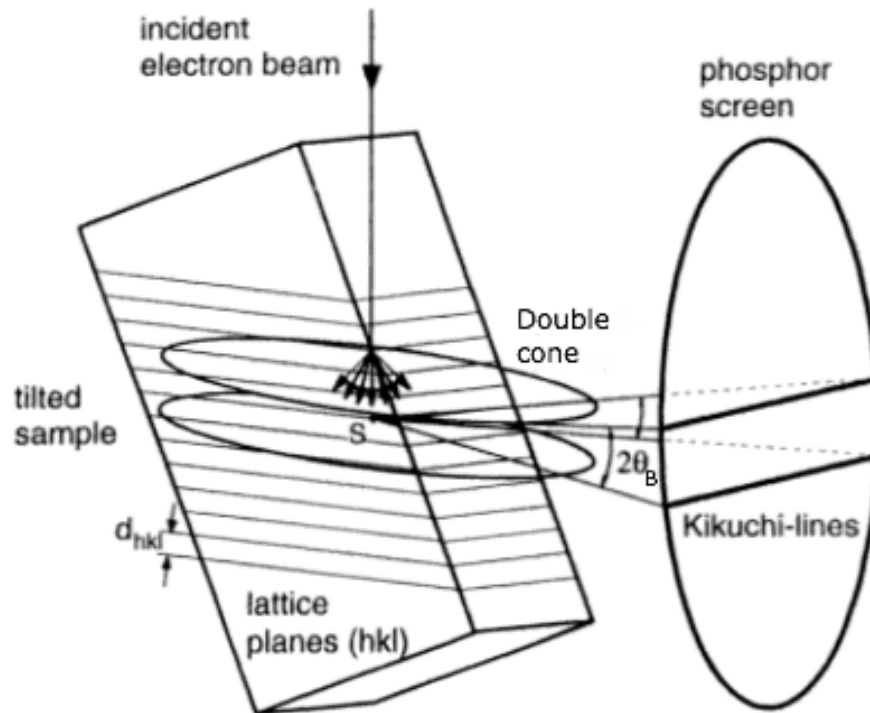


Figure 2.8: The electron backscattering mechanism and pattern formation [78].

### 2.2.5 Design of a scanning electron microscope

A scanning electron microscope consists of three major parts: an electron gun, a beam focusing system and a specimen chamber. A simplified schematic of an SEM is shown in Fig. 2.9.

The electron gun, which is placed at the top of a column, provides a stable source of electrons necessary to produce an electron beam, and accelerates the electrons to an energy of 1-30 keV. While the first electron guns used in SEMs relied on thermionic electron emission from tungsten or lanthanum hexaboride filaments, modern microscopes are equipped with field emission guns which have longer lifetime, high beam current and a smaller electron spot size. Furthermore, field emission guns have a lower energy spread of 0.3 eV (as compared to a 1-2 eV spread typically achieved by thermionic emission guns), which improves the resolution of SEM images by substantially reducing chromatic aberrations. However, field emission guns require ultrahigh vacuum to prevent contamination and stabilise the electron emission [75,76].

The electron beam produced by the gun is further demagnified and focused on a specimen by a set of electromagnetic lenses and apertures. Typically, SEMs have two types of electron lenses: a condenser lens and an objective lens. Two or more objective lenses and their aperture collimate an otherwise diverging beam and filter out inhomogeneous and scattered electrons,

consequently minimising spherical aberration. Then, objective lenses demagnify the beam down to a diameter of 2-10 nm and focus it onto the surface of the specimen. Also, two additional orthogonal pairs of coils are placed in the column in order to deflect the beam and scan the specimen [75, 76].

A specimen chamber is normally kept at a high vacuum to prevent scattering of the electron beam. It contains detectors and a specimen stage, which allows the specimen to be tilted by large angles and moved both laterally and longitudinally to the electron beam [76].

## 2.3 Chemical vapour deposition

### 2.3.1 Introduction

Chemical vapour deposition (CVD) is a technique used to synthesise thin solid films on substrate materials from film-forming species produced in chemical reactions of precursors. Being designed in the 19th century, its application has gained momentum with the development of the microelectronics industry since the 1970s. Nowadays, CVD processes are used to produce thin, high-purity and large-area films with desirable properties for solid-state electronic devices, cutting tools, nuclear reactors and rocket engine components [40, 79].

There exist a few types of CVD processes based on the way chemical reactions are initiated. Typically, high-quality thin films are formed from species that have high mobility on the surface of a substrate; therefore, thermal energy is supplied either to the CVD reactor or to the substrate, with deposition temperatures often reaching over 800°C. However, deposition on temperature-sensitive substrates requires a different method for energy supply. A reduction of growth temperature to below 300°C can be achieved using a plasma-enhanced CVD process, in which gas-phase precursors are decomposed into ions, electrons, free radicals, etc., as a result of an electric current discharge. Then, further chemical reactions occur between the component species leading to layer formation on a substrate [79]. Another method to deposit a layer is through a photo-assisted CVD, which employs a focused laser beam either to create local heating on a substrate or to induce photolytic reactions in a precursor [40].

CVD processes can also be differentiated according to the operating pressure (such as low-pressure CVD or atmospheric pressure-CVD) and both physical and chemical nature of the precursor gases. One of the most notable examples of the latter is metalorganic CVD, which is particularly important in deposition of epitaxial compound semiconductor materials [79].

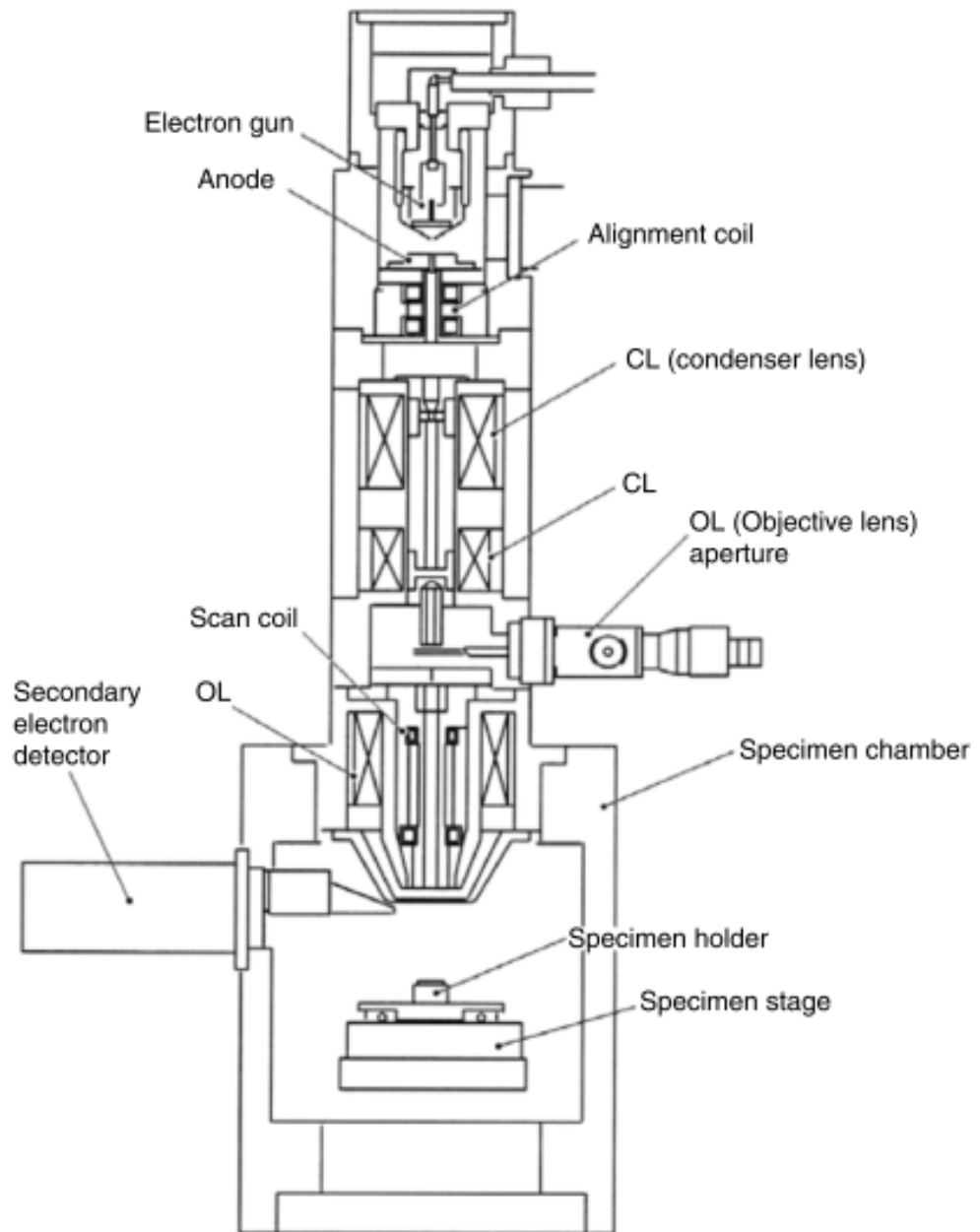


Figure 2.9: A schematic of an SEM construction [75].

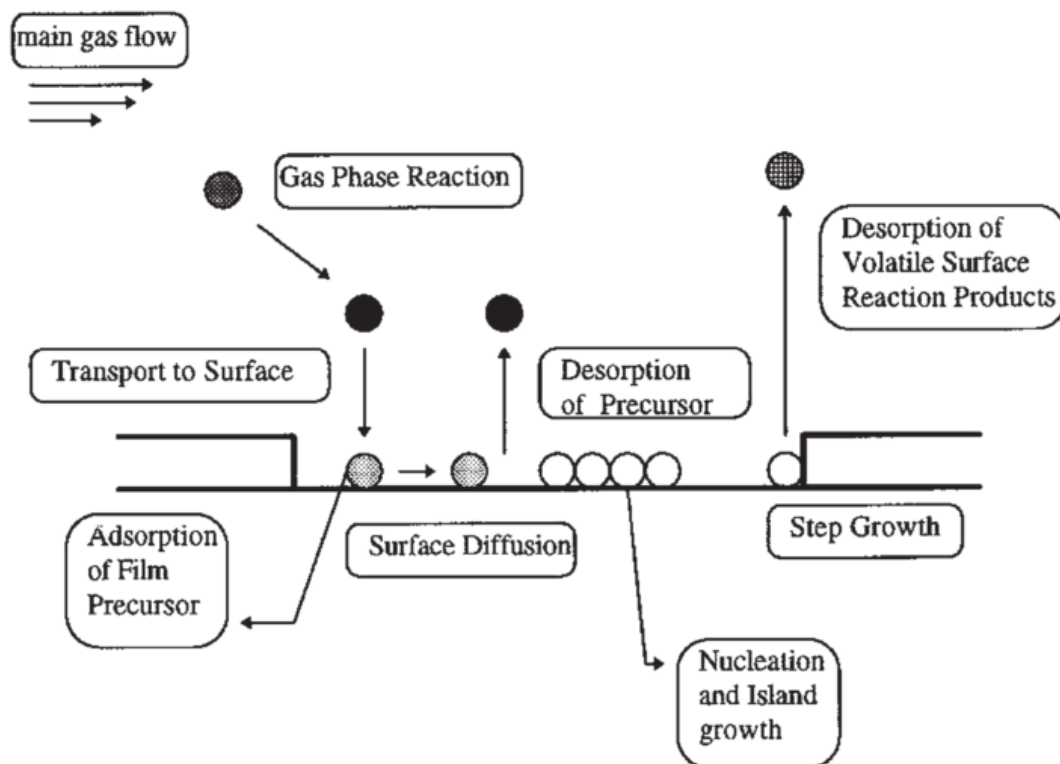


Figure 2.10: A schematic of the stages in CVD growth of thin films [40].

### 2.3.2 The CVD Process

A vast majority of CVD processes, independent of their type, incorporate the major physicochemical steps depicted in Fig. 2.10. Firstly, precursor gases are transported to the CVD reactor with the bulk gas stream. Then, gas-phase reactions are initiated by one of the methods mentioned above, resulting in a production of intermediate and/or film-forming species. Assuming a laminar flow of reactants, a stagnant boundary layer, often of non-uniform thickness, forms adjacent to the substrate surface. As the reactants are transported through the boundary layer, their velocity drops to zero and adsorption at the surface takes place. The reactants further diffuse, which is followed by nucleation at active sites, surface chemical reactions and desorption of volatile reaction products [40]. Depending on the precursor amount and the length of exposure, the nuclei grow laterally until they merge into a continuous film and/or form multilayer structures.

A CVD process can be active in one of two kinetic regimes: surface reaction limited and mass transport limited. The dominant regime depends on the overall process conditions. A surface reaction limited regime is typically active at low growth temperatures or low pressures. In the former case, a substantial number of chemical reactions cannot be initiated due to an

insufficient amount of energy supplied to the system, while in the latter case, a surplus of reactive species is transported to the substrate surface as a result of an enhanced diffusivity at low pressures [79]. A mass transport limited regime, on the other hand, dominates at high temperatures and high pressures; therefore, depletion of reactive species on the substrate surface can be observed due to a high rate of surface reactions and reduced diffusivity through the boundary layer.

### 2.3.3 CVD of graphene on copper substrates using methane

The graphene formation mechanism and therefore film morphology is highly dependent on the substrate qualities. Catalytic materials, such as transition metals, boost the growth of graphene by aiding dehydrogenation of adsorbed hydrocarbon precursors. The extent of their catalytic activity can be evaluated by comparing activation energy barriers for sequential detachment of hydrogen and carbon species from the initial state of the precursor until a completely dissociated molecule is obtained [80, 81]. The calculated dissociation energy of methane, which is used as a precursor for graphene growth in this thesis, can vary between 0.05 eV (on Ni(100)) to 5.63 eV (on Au(111)) [56]. On substrates with low dissociation barrier (like Ni, Pd, Rb or Co), the methane decomposition product is mostly atomic carbon, while complete dehydrogenation on substrates with high activation energy (like Au or Cu) is energetically unfavourable [56]. In the latter case, it is thought that methane decomposes into partially dehydrogenated species, such as  $\text{CH}_i$  ( $i=1, 2, 3$ ), which combine together and dehydrogenate in later stages of film growth [80].

Among many transition metals suitable for graphene growth, considerable interest has been focussed on polycrystalline copper - an inexpensive catalytic substrate material which promotes the formation of predominantly single-layer graphene films [41]. Its distinctive feature is low carbon solubility, which induces surface mediated growth and suppresses the formation of multilayers and defects. In contrast, substrates with higher carbon solubility such as nickel, give a substantially higher fraction of graphene multilayers due to a different growth mechanism based on carbon dissolution and precipitation out of the substrate upon cooling [82]. Furthermore, copper and graphene interact through a "soft" bond which forms as a result of a charge transfer between a partially filled 4s orbital of copper and a  $\pi$  orbital of graphene. Due to the weakness of this interaction and a mismatch in thermal expansion coefficients of the materials, graphene forms wrinkles as a way to relax the compressive strain caused by shrinking copper upon cooling [83].

Before graphene growth, copper substrates are usually pretreated in a variety of solvents to remove contaminants from the surface and annealed in an argon and hydrogen atmosphere which reduces the native oxide layer and hence increases the catalytic activity. Annealing at high temperatures also improves copper surface morphology and increases copper grain size [82]. Graphene films are typically grown at temperatures between 1000°C and the melting point of copper at 1084.62°C [84]. Morphological parameters of graphene flakes such as size, shape and nucleation density are determined by particular substrate pre-treatment procedures and growth conditions like temperature, partial precursor pressure and overall pressure in a CVD reactor.

The growth of large single-crystalline graphene islands is limited by their nucleation density, which is remarkably different between LPCVD and APCVD. The pressure in a CVD reactor affects most of the growth processes depicted in Fig. 2.10; however, the major difference arises in desorption of carbon species from the substrate surface [46]. At lower pressures, the rate of desorbed species returning to the surface due to collisions with the gas in the diffusion layer is 3 orders of magnitude lower than at higher pressures. Moreover, in LPCVD, substrates tend to evaporate at fairly high rates ( $\leq 4 \mu\text{m/h}$  at 1000°C for copper), which in turn boosts the desorption of carbon species and further reduces the nucleation density of graphene domains [46].

Even though the graphene nucleation density is lower in LPCVD, APCVD has emerged as a preferable method for industrial scale production of graphene films. The latter adopts cheaper, more basic equipment and eliminates the negative effects associated with copper evaporation such as formation of irregularly shaped dendritic graphene domains and an increase of their defect density [46,85]. Fig. 2.11 (a) and (b) show four- and six-lobed graphene islands respectively grown at low pressures while (c) shows hexagonal graphene structures grown at atmospheric pressure. Micro-Raman mapping of the islands revealed that  $I_D/I_G$  values, which indicate the extent of defects, were  $\sim 0.4$  for the dendritic islands, while the ratio went down to  $\sim 0.2$  for the hexagonal islands. [85].

The size and nucleation density of graphene islands grown by APCVD can be altered by optimisation of the growth temperature and a partial precursor pressure. At a fixed  $\text{CH}_4$  concentration of 20 ppm hardly any graphene can be grown at temperatures below 850°C even after an hour of exposure to precursor, while at temperatures ranging between 900°C and 1000°C the growth of bi- and few-layer graphene is observed [47]. At higher temperatures, graphene grains are mostly one layer thick and merge into a homogeneous film after a 30 min

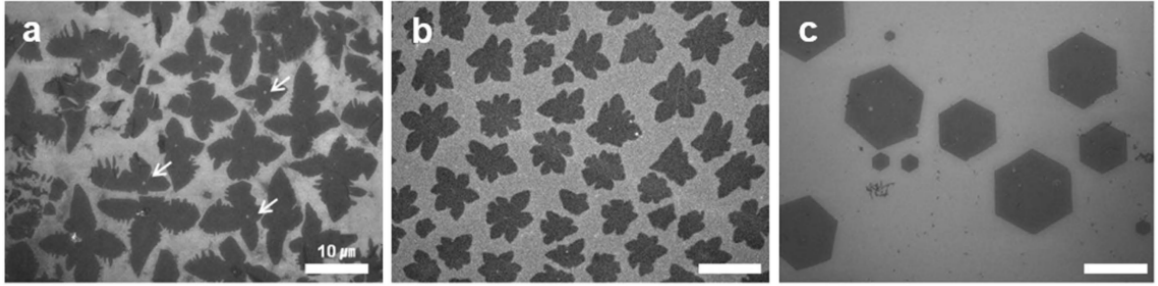


Figure 2.11: SEM images of graphene islands grown at low pressures (a), (b) and atmospheric pressure (c). White arrows in (a) mark small holes observed at central parts of the four-lobed islands and the scale mark in the images represents 10  $\mu\text{m}$  [85].

growth. In addition, it was observed that higher growth temperatures reduced nucleation density and led to a formation of larger graphene domains [47]. A study on the effect of a partial precursor pressure has showed that samples synthesised at 5-30 ppm of  $\text{CH}_4$  at  $1050^\circ\text{C}$  have higher nucleation densities at higher  $\text{CH}_4$  concentrations with monolayers dominating at 5-10 ppm concentrations and bilayers at higher concentrations [44].

Graphene morphology can also be changed by varying hydrogen to precursor [86] and hydrogen to argon [87] concentration ratios, as well as copper annealing time [88] and introducing cyclic precursor exposure [89]; however, these are beyond the scope of the work reported here and therefore will not be discussed in detail.

#### 2.3.4 CVD systems

CVD systems are very diverse in terms of reactor design and a type of precursor delivery system. While many CVD tools used in industrial facilities have very sophisticated designs that optimise their processing flexibility and performance in order to give molecular-scale control of processes in a reaction chamber, much research is conducted using much simpler, often home-made tools [40]. Nonetheless, all CVD systems have three prevalent features: precursor transport system, reaction zone and an exhaust system. This section briefly overviews the main components and equipment design of thermal research-scale reactors.

Most research CVD reactors are fairly small, constructed to accommodate samples up to a few centimetres in size and minimise precursor usage. Thermal reactors are classified into two categories, hot-wall and cold-wall, depending on the way in which thermal energy is given to the system. In hot-wall reactors, the entire reaction chamber is surrounded with resistance elements, while in cold-wall reactors only a substrate is subject to either inductive or radiant

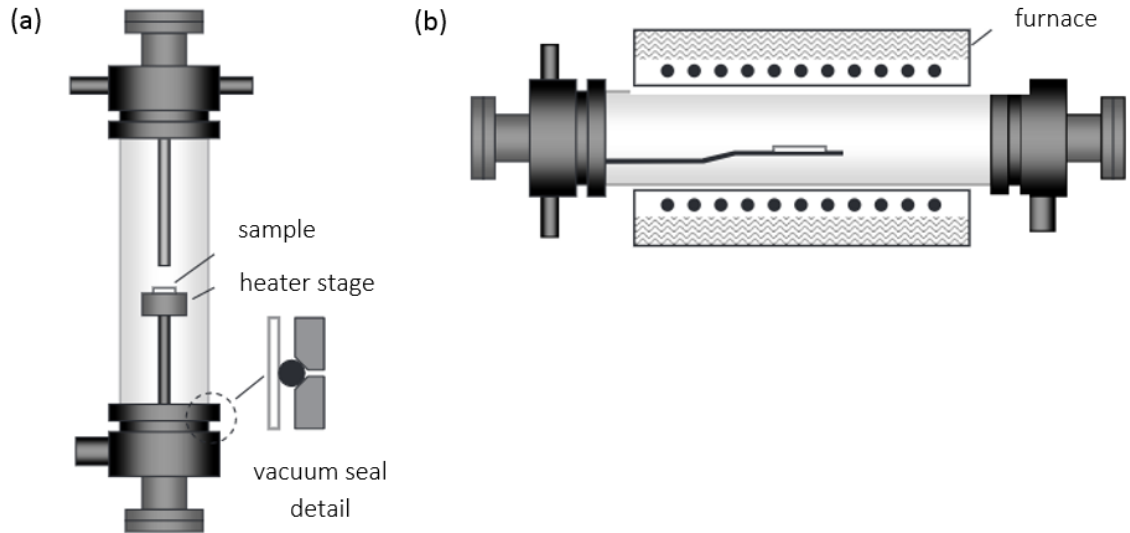


Figure 2.12: A scheme of a vertical cold-wall CVD reactor (a) and a horizontal hot-wall reactor [40].

heating. These reactors are typically found in tubular configurations and can operate at pressures ranging from atmospheric to ultra-high vacuum with the help of pumps. Fig. 2.12 (a) shows a vertical tube reactor in which a sample is placed on a heated stage and (b) a horizontal reactor in which the deposition zone is enclosed in a tube furnace [40].

A successful film deposition process is highly dependent on the precursor delivery system. The delivery method is usually determined by the state of reactive species, whether they are gaseous, liquid or solid. The most common approach for the transport of gaseous reactants is to use cylinders containing the necessary precursors and mass flow controllers (MFCs), which control partial concentrations of gases [90]. For the liquid precursors, MFCs can be used together with a vaporiser or a bubbler which saturates carrier gas with a precursor. The transport of solid state precursors is slightly more complicated due to their high vapourisation temperatures; therefore, it is common to generate reactive species *in situ* by, for instance, reduction reactions [91].

Deposition of certain films may often require the use of toxic, flammable or corrosive precursors. Hence, CVD systems are equipped with exhaust systems to safely dispose of dangerous residual precursors or reaction by-products. Depending on particular reactions, the exhaust system may include a particle trap which collects droplets and gases, incinerating systems and a variety of pumps together with demisters and scrubbers [91].

**2.3.5 Summary**

This chapter provided a comprehensive description of the theory underpinning Raman spectroscopy, SEM and EBSD, which were extensively used to characterise grown graphene samples. Also, a detailed description of graphene growth by CVD was presented.

## Chapter 3

# Experimental instrumentation and sample preparation

This chapter outlines the sample preparation procedure and describes the equipment used for graphene growth and characterisation.

### 3.1 CVD system for graphene growth

The analysis of graphene presented in this thesis was carried out on samples grown in a home-made hot-wall CVD system, illustrated in Fig. 3.1, at atmospheric pressure. The system consists of a Vecstar furnace heated by a wire element wound around a ceramic tube of 15 mm inner diameter [92]. The furnace is equipped with a K-type thermocouple and a PID controller, CAL 9500, which can be programmed to run heating processes consisting of a large number of heating and cooling stages with distinct ramp rates, dwell times and with temperature set-points ranging between ambient temperature and 1200°C [93]. The substrate for graphene growth is placed in a quartz tube of inner diameter of 10 mm, which is then inserted into the furnace so that the position on the substrate would coincide with the furnace's hot-spot. One end of the quartz tube is connected to cylinders containing CH<sub>4</sub> and 5% H<sub>2</sub>/Ar and the gas flow is regulated by mass flow controllers (MFC), Tylan FC-2900MEP, and an MFC switch box, Tylan RO-28. The MFCs are set to supply a desired concentration of gases into the CVD system for required intervals of time during sample growth. The gas exiting the tube is directed to a gas bubbler filled with oil, which prevents the backflow of atmospheric gases into the chamber, and then exhausted through a fume hood.

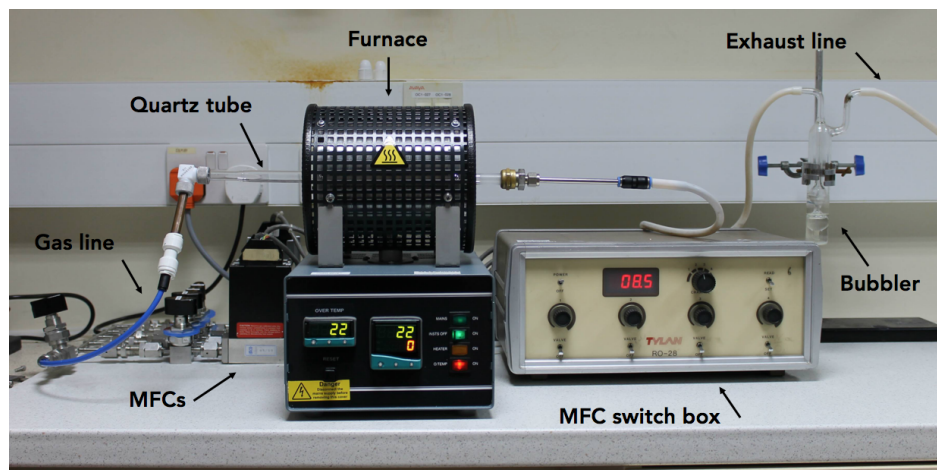


Figure 3.1: CVD system used for graphene growth.

### 3.2 ASEQ Instruments Rm1 Raman spectrometer

The Raman spectra of the graphene samples were taken by an ASEQ Instruments Rm1 Raman spectrometer, shown in Fig. 3.2. The instrument consists of a low noise 532 nm laser, a focusing 10x objective lens with 10 mm working distance, Semrock long-wave pass filter, which absorbs all light up to 537 nm transmitting only Stokes scattered light, and an HR1-T spectrometer with a thermoelectrically cooled 3648 pixel charge coupled device (CCD) [94]. The system is also equipped with a laser control switch box and a motorised sample stage allowing XYZ translation.

For the measurements of Raman spectra, graphene samples were mounted on a sample stage and probed by a 4 mW power laser beam (measured at a sample). The data was recorded using a specialised ASEQ software and calibrated with respect to a previously recorded Raman spectrum of SiC in order to determine precise Raman shift values at which graphene peaks occur. Due to the nature of the samples, the obtained graphene Raman spectra included the Cu fluorescence background, which was removed at later stages of data analysis.

### 3.3 FEI Helios Nanolab 600 DualBeam system

The imaging of graphene samples and crystallographic analysis of Cu foils was carried out using an FEI Helios Nanolab 600 focused ion beam (FIB) and scanning electron microscopy system, depicted in Fig. 3.3. The instrument can operate in ion beam and electron beam regimes, each of which has its own set of applications; however, for the work presented in this thesis, only the electron beam imaging mode was used.

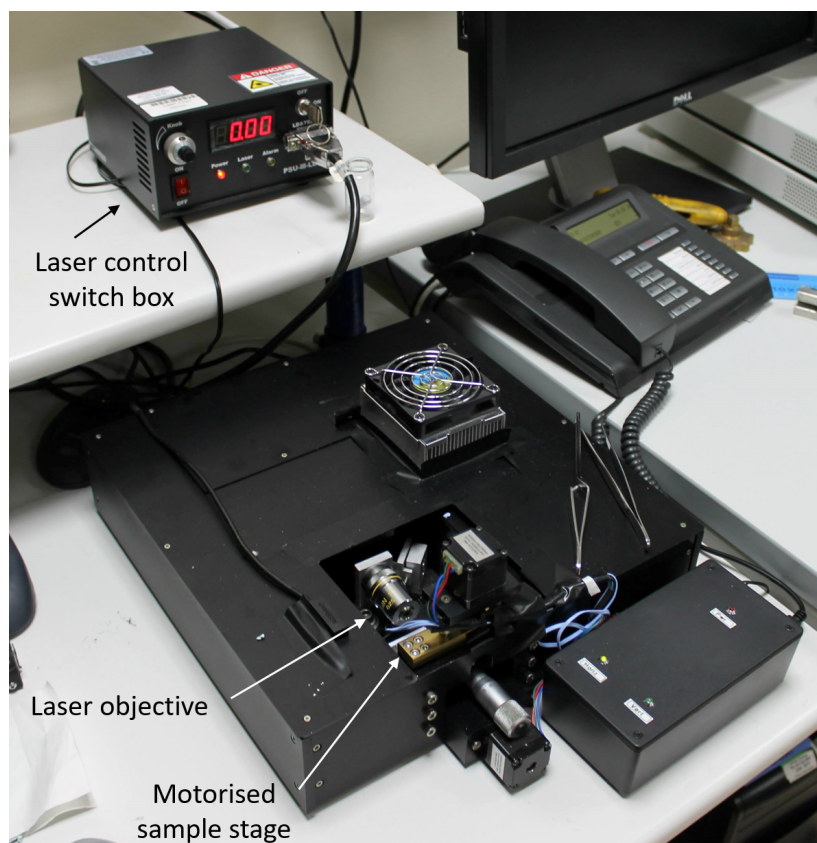


Figure 3.2: ASEQ Instruments Rm1 Raman spectrometer used for graphene characterisation.

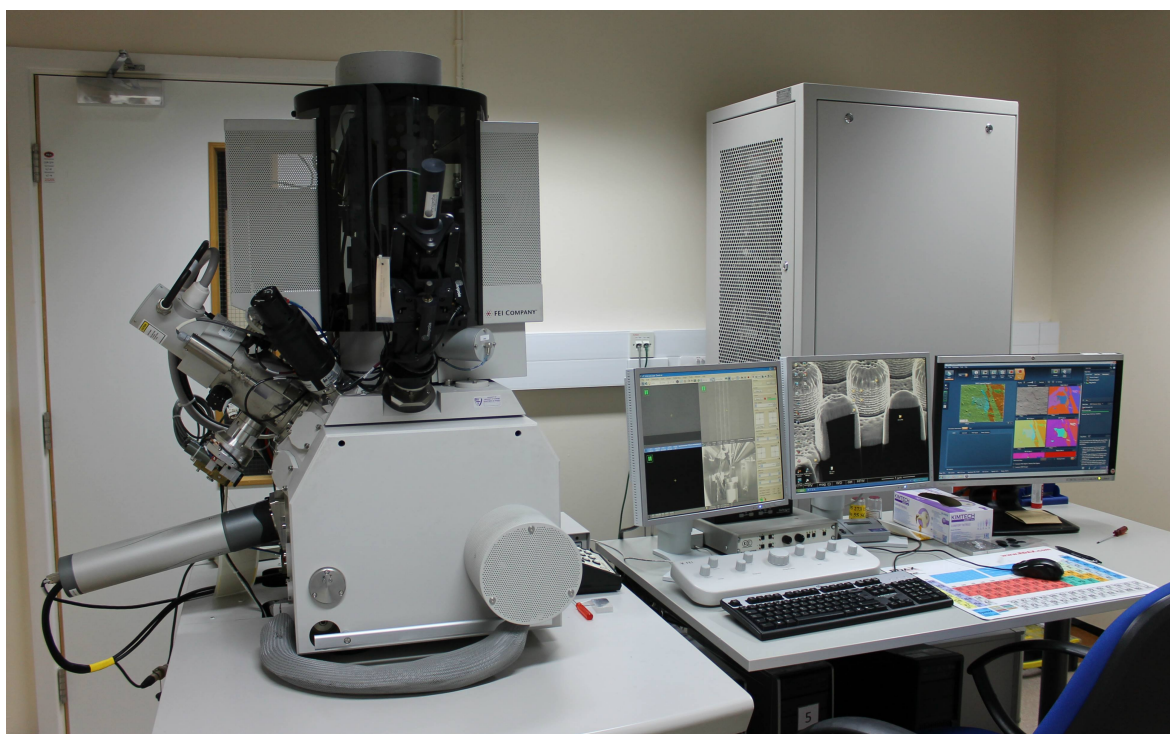


Figure 3.3: FEI Helios Nanolab 600 DualBeam system.

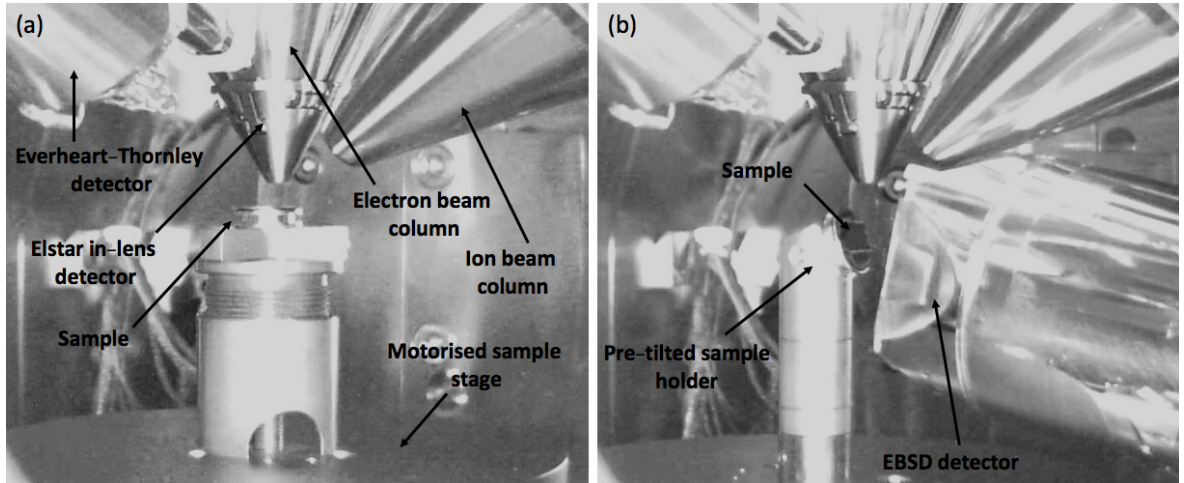


Figure 3.4: Imaging (a) and EBSD (b) in FEI Helios Nanolab 600 DualBeam system.

For the imaging of graphene islands, samples are mounted on a high precision 5-axis motorised stage, placed under the electron column, as shown in Fig. 3.4(a). In SEM mode, the system probes a sample with an electron beam produced by a Schottky-type field emission gun located at the top of the electron column. It consists of a very sharp conductive needle which emits thermionic electrons, while an electric field induced at its tip enhances the emission by reducing the work function that has to be overcome in order to free the electrons [73]. The resulting electron beam is then accelerated by an electric field and focused at the sample surface by electromagnetic lenses. The beam current produced by the Helios Nanolab system can reach up to 22 nA with incident beam energies ranging between 0.2-30 keV and a resolution of 0.9 nm at 15 kV accelerating voltage [95]. For imaging purposes, the graphene samples were probed using a beam energy of 3 keV and current of 0.17 nA. The secondary electrons (SE) arising from the beam-specimen interactions were collected by Everhart-Thornley and Elstar in-lens SE detectors [95].

The FEI Helios Nanolab system was also used to carry out electron backscattering diffraction (EBSD) measurements and map the crystallographic orientation of the Cu substrate. As the backscattered electrons (BSE) are emitted at large angles, the sample was placed on a specialised sample holder pre-tilted by  $70^\circ$  from the horizontal, pictured in Fig. 3.4(b). The foil was probed by a 30 keV electron beam at a current of 2.7 nA and the BSEs were collected by a Nordlys EBSD detector [96] brought close to the sample. The mapping process is controlled by AZtec software, which matches the solutions representing different crystallographic orientations of a pre-selected crystal with the Kikuchi patterns arising from the diffracted electrons. The relevant part of a recorded dataset contains a secondary electron

image obtained using a standard imaging technique, an EBSD map, every point of which expresses the crystallographic orientation of the substrate in terms of Euler angles, and an optional forward scattered electron (FSE) image produced from an FSE detector. The data is further analysed using Tango and Mambo software [97] which transform the Euler angle data into pole figures and allow the Miller indices of the surface planes to be determined.

### 3.4 Sample preparation

The graphene samples were grown on 99.9% purity, 0.2 mm thick Cu foils obtained from Advent Research Materials Ltd and cut into 10 x 7 mm<sup>2</sup> rectangles. The substrates normally contain surface particulate contamination such as Si, O, Fe, Ca, Ce, Ru, and Pt, as identified by other research groups using energy-dispersive x-ray spectroscopy and Auger electron spectroscopy [98,99]. It is thought that these nanoparticles create a lower graphene nucleation energy barrier and therefore act as island nucleation sites, consequently increasing graphene nucleation density to undesirable levels, promoting the formation of multilayer islands and degrading graphene's electrical properties [99,100]. On the other hand, some studies suggest that only particles of certain size can act as nucleation sites (>20 nm in diameter under particular experimental conditions) and explore a "seeded" growth of subcentimetre graphene flakes on mildly oxidised copper [101]. Nonetheless, in order to minimise the negative effects associated with surface contamination, the as-received foils were subjected to a following cleaning procedure: (i) foil sonication in acetone for 10 min to remove organic impurities, (ii) sonication in isopropyl alcohol for 10 min to remove residual acetone, (iii) foil treatment with acetic acid for 30 s to reduce the native oxide layer, (iv) rinsing in ultra-high-purity water and (v) drying under a nitrogen stream.

Together with surface contaminants, the as-received foils also contain morphological defects such as striation marks, pits, bumps, grain boundaries and scratches. It has been found that these defects result in a significant increase in nucleation density of graphene domains near the defective sites and therefore play a detrimental role in the growth of large monolayer graphene domains [102]. To reduce the amount of surface defects, the cleaned substrates were annealed in the CVD system for 3 hours at 1065°C and 1025°C, corresponding to the temperatures used for the subsequent graphene growth. The thermal treatment was carried out in H<sub>2</sub>/Ar atmosphere supplying the gas mixture to the quartz tube at a rate of 300 sccm throughout the entire process. The use of predominantly argon atmosphere (95%) ensures an inert environment during annealing of the substrate, which would otherwise rapidly oxidise

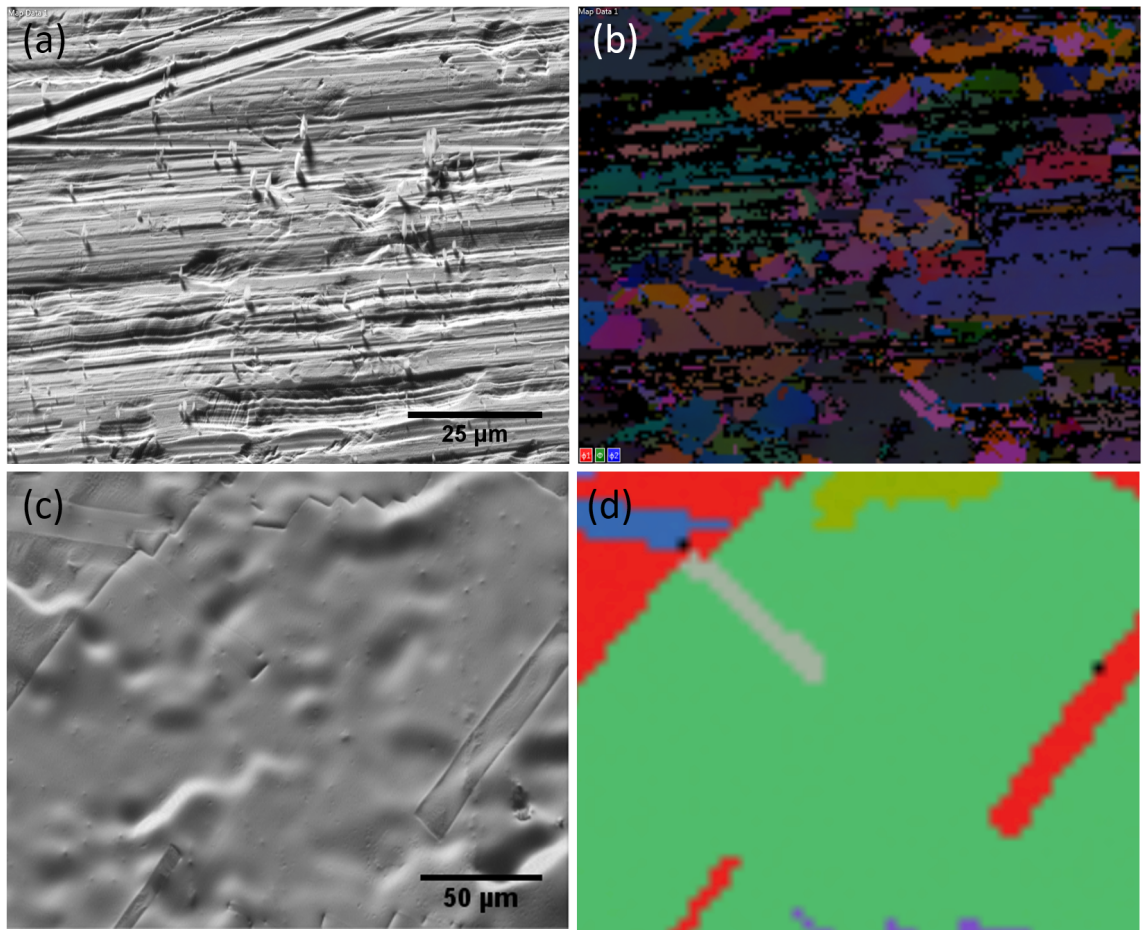


Figure 3.5: Forward scattered electron images and EBSD maps of Cu surface before and after the treatment, (a)-(b) and (c)-(d) respectively.

at high temperatures, while a low concentration of hydrogen reduces any remaining oxide on the Cu surface and aids the surface smoothing process [87]. The effect of substrate cleaning and annealing is shown in Fig. 3.5, which depicts Cu surface before and after the treatment. Evidently, the substrate in (a) contains a number of contamination particles, deep striation marks and scratches, with the corresponding EBSD map in (b) indicating that the surface consists of small irregular grains. The treated sample in (c), on the other hand, has much lower surface roughness and significantly larger grains as shown in (d)

After annealing,  $\text{CH}_4$  gas was immediately introduced into the CVD system at a flow rate of 1 sccm, while maintaining the same system temperature and the flow of  $\text{H}_2/\text{Ar}$  gas. In order to investigate the changes in the resulting graphene coverage, the  $\text{CH}_4$  was passed for a number of different time intervals ranging between 60 s and 94 s. After the growth, the furnace was switched off and the sample was left to cool naturally under the stream of  $\text{H}_2/\text{Ar}$

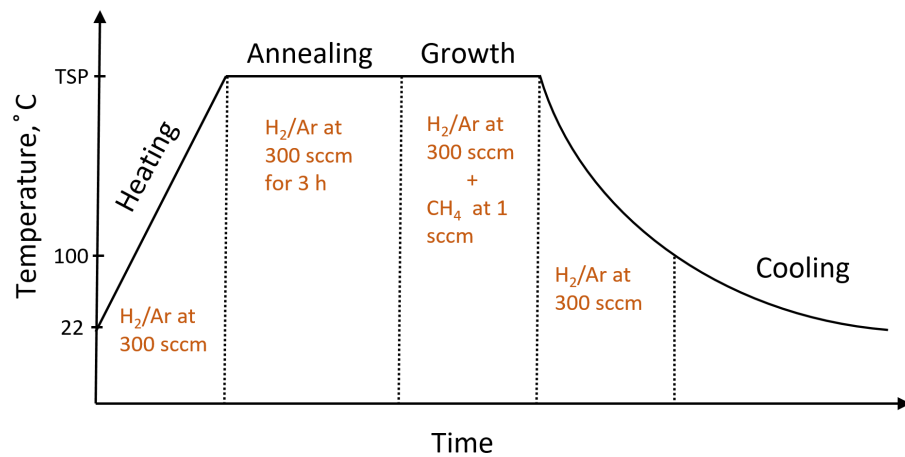


Figure 3.6: Graphene growth cycle (TSP refers to a temperature set-point of 1065°C and 1025°C).

gas until its temperature dropped to 100°C and the oxidative etching of graphene islands at high temperatures could be avoided. The overall growth cycle in the CVD system is presented in Fig. 3.6.

### 3.5 Summary

This chapter briefly discussed the CVD system and the procedure used to grow graphene samples. It also overviewed the sample characterisation equipment: ASEQ Instruments Raman Rm1 spectrometer and FEI Helios Nanolab DualBeam 600 system, which were used to obtain Raman spectra, images and EBSD maps of the samples.

## Chapter 4

# The kinetics of graphene growth on copper and its influence on island morphology

This chapter presents the results of graphene growth by CVD on polycrystalline Cu foils using  $\text{CH}_4$  as a precursor. The analysis includes SEM and Raman characterisation of graphene islands, interpretation of the global coverage evolution in terms of modified JMAK and modified Gompertz models, and a discussion of Cu grain-dependent differences in island morphology and coverage.

### 4.1 Introduction

As discussed in Section 1.3, a number of graphene production routes have been explored aiming to synthesise large-area, high-quality graphene films. Over the last decade, CVD has emerged as one of the most widely applied techniques, offering a scalable and relatively inexpensive way to produce graphene films with a controllable grain size, nucleation density, number of layers and defect density [46,103,104]. The CVD process is typically very sensitive to a number of experimental variables including growth pressure, temperature, morphological features of the substrate, type and concentration of carbon precursor and use of auxiliary gases such as hydrogen. Therefore, a careful optimisation of the growth conditions and substrate cleaning procedures is necessary in order to obtain graphene films with desirable properties.

Nowadays, CVD growth of graphene is most commonly carried out using transition metal substrates and hydrocarbon precursors. Generally, transition metals catalyse the dehydrogenation of the precursor and, depending on their carbon solubility, support either bulk-mediated or surface-mediated graphene growth. While the former mechanism typically leads to formation of multilayers, the highest fraction of monolayer material can be achieved by surface-mediated growth [41, 82]. Particular interest has been focused on copper substrates due to their low carbon solubility and resultant self-limiting growth of graphene monolayers under certain experimental conditions. A variety of precursors have also been explored due to different decomposition pathways of each material providing different graphene growth mechanisms. One of the most extensively examined precursors has been methane, which has the lowest dehydrogenation energy among other frequently used gaseous hydrocarbons and a low pyrolysis rate giving a better control over film uniformity and the number of deposited layers [105].

Further improvements to graphene quality can be made through studies of growth kinetics, which can give information on the nature, speed and activation energies of the phase transformation processes occurring during CVD growth. Hence, a number of kinetic models have been developed in order to explain the behaviour observed in graphene growth. So far, modified JMAK [51] and Gompertz [57] models have been debated the most; however, they involve contradicting sets of assumptions, which lead to different explanations of graphene growth on copper. As mentioned in Section 1.4, the JMAK model is based on supersaturation of the substrate surface with active carbon species, which initiates the nucleation of stable graphene domains. Their growth proceeds via the attachment of adsorbed carbon species until the concentration of the latter drops from a critical supersaturation level to the equilibrium level [51]. An important assumption underpinning the JMAK model is that no additional precursor dissociation occurs after the domain nucleation, which is dubious in the context of graphene growth by CVD. On the other hand, the modified Gompertz model suggests that island nucleation starts when the surface concentration of carbon species reaches a critical supersaturation level, and the growth of the nuclei is sustained by a continuous supply of a precursor [57]. It appears that the Gompertz model could provide a better framework for interpretation of graphene growth than JMAK; however, in the literature, the models are fitted to very small data sets giving, at best, just one degree of freedom, and therefore must be considered as inconclusive.

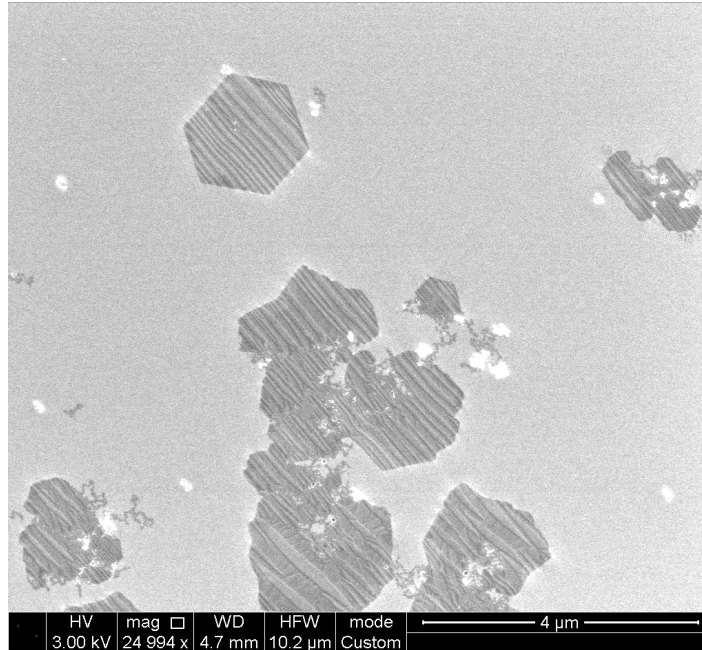


Figure 4.1: Graphene islands on Cu.

## 4.2 Experimental

The graphene samples produced in this work were grown on  $10 \times 7 \text{ mm}^2$ , 0.2 mm thick polycrystalline Cu foils (Advent Research Materials Ltd) which were cleaned and treated with acetic acid according to the procedure outlined in Section 3.4. The samples were then quickly placed into the CVD tube furnace in order to minimise their exposure to oxygen and contaminants in the air and annealed at temperatures of  $1025^\circ\text{C}$  and  $1065^\circ\text{C}$  in argon gas containing 5% hydrogen, flowing through the system at a rate of 300 sccm. Immediately after annealing, methane was introduced into the quartz tube to initiate graphene growth, which consists of a number of stages including adsorption and dehydrogenation of  $\text{CH}_4$  on the Cu surface, followed by diffusion of the carbon species, their nucleation and subsequent growth. Monolayer graphene is typically obtained by passing through a very small partial pressure of the precursor compared with that of the carrier gas, for extended periods of time, as shown in the literature; therefore, a  $\text{CH}_4$  flow rate of 1 sccm was chosen as the lowest flow rate consistently maintainable by the MFCs available. After the growth, the heating of the furnace was switched off and the sample was left to cool naturally under the  $\text{H}_2/\text{Ar}$  stream for approximately 3 hours. A SEM image of as-grown graphene is presented in Fig. 4.1. Here, darker patches represent graphene islands, while the lighter background shows the oxidised copper surface which is exposed to the atmosphere during sample handling after growth.

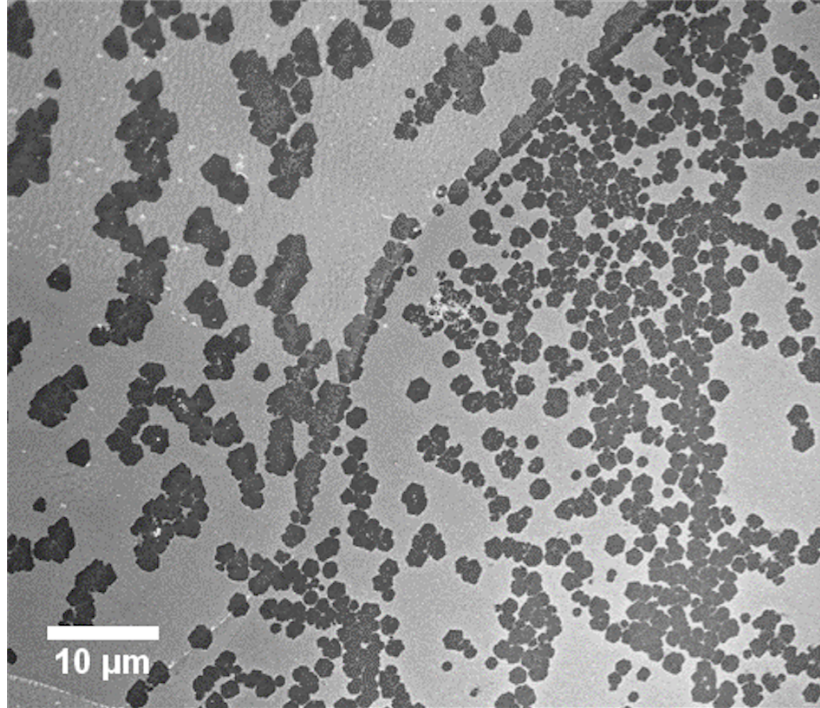


Figure 4.2: Differences in island growth on different Cu faces.

As graphene acts as a protective layer preventing copper oxidation, one can clearly see the morphological features of the Cu substrate such as step bunches through the graphene film.

In order to investigate the kinetics of graphene growth on Cu, a set of samples was produced at 1065°C with CH<sub>4</sub> flow times ranging between 60 s and 94 s. After growth, the samples were characterised by Raman spectroscopy, which provided information on the quality of the graphene, as discussed in Section 2.1. In order to track the evolution of graphene coverage over time, SEM was employed in imaging mode, which is discussed in greater detail in Section 2.2. During analysis of the resulting micrographs, a few subtle copper grain-dependent differences in graphene island growth and morphology were noticed: as shown in Fig. 4.2, certain grains supported a sporadic growth of graphene domains with a quite high nucleation density, while others seemed to produce ordered graphene structures consisting of chains of graphene islands nucleating at lower densities. As the Cu surface is highly energetic at very high growth temperatures, close to the Cu melting temperature of 1084.62°C [84], with nearly vanishing differences between morphologies and orientations of the grains at their surface, several graphene samples were produced at 1025°C to examine the influence of the substrate texture on the graphene growth further. The rationale behind the reduction of the growth temperature was to stabilise the substrate surface and amplify the impact of the Cu foil texture on graphene nucleation and growth. The samples were then probed by SEM in the

EBSDF mode in order to identify the crystallographic orientations of the Cu grains under the graphene islands.

## 4.3 Results and discussion

### 4.3.1 Characterisation of graphene samples

As outlined previously, graphene samples were produced using  $\text{CH}_4$  as a precursor, which was introduced into the CVD system at a flow rate of 1 sccm together with 300 sccm of 5%  $\text{H}_2/\text{Ar}$  gas for 60-94 s at a set temperature of  $1065^\circ\text{C}$ . A total of nine samples were prepared in order to track the changes in graphene areal coverage and determine a clear trend from the earliest moments of island growth to the point a saturated coverage is reached. The coverage curve, shown in Fig. 4.3(a), was obtained by applying a standard thresholding technique to multiple SEM images obtained from each sample. SEM micrographs of samples grown at 60, 67, 80 and 87 seconds  $\text{CH}_4$  exposure, representing the graphene domains at the initial, intermediate and late stages of growth are shown in Fig. 4.3(b), (c), (d) and (e) respectively. It is evident that despite the substrate pre-treatment procedures the nucleation density of the islands is quite high, with the majority of domains starting to merge before a substantial coverage is reached. However, the merging of domains is fairly insignificant on samples grown at  $\text{CH}_4$  flow times of 60 s and 63 s, which have nucleation densities of  $0.020 \pm 0.002$  and  $0.015 \pm 0.001$  islands per  $\mu\text{m}^2$  respectively. Furthermore, at short growth time, the great majority of domains on each sample have very similar sizes, suggesting that graphene predominantly grows via the capture of adsorbed carbon species rather than continuous nucleation of new islands. It was also observed that at short and intermediate growth times the islands exhibit compact hexagonal or nearly circular shapes indicating deposition in a mass transport limited regime [106]. However, at longer growth times the islands tend to develop irregular shapes and dendritic edges, as shown in Fig. 4.3(d) and (e), which was previously thought to happen only at low pressure growth, due to significant copper evaporation [85]. The observed morphological differences at atmospheric pressure could potentially arise due to interactions between neighbouring islands at their interface upon merging or due to anisotropic diffusivity of reactive carbon species over the copper surface, with the variations in the latter being influenced by surface contaminants, non-uniform surface roughness or the crystallographic orientation-dependent morphological structure of copper grains.

The samples were also analysed by Raman spectroscopy, the details of which are described in

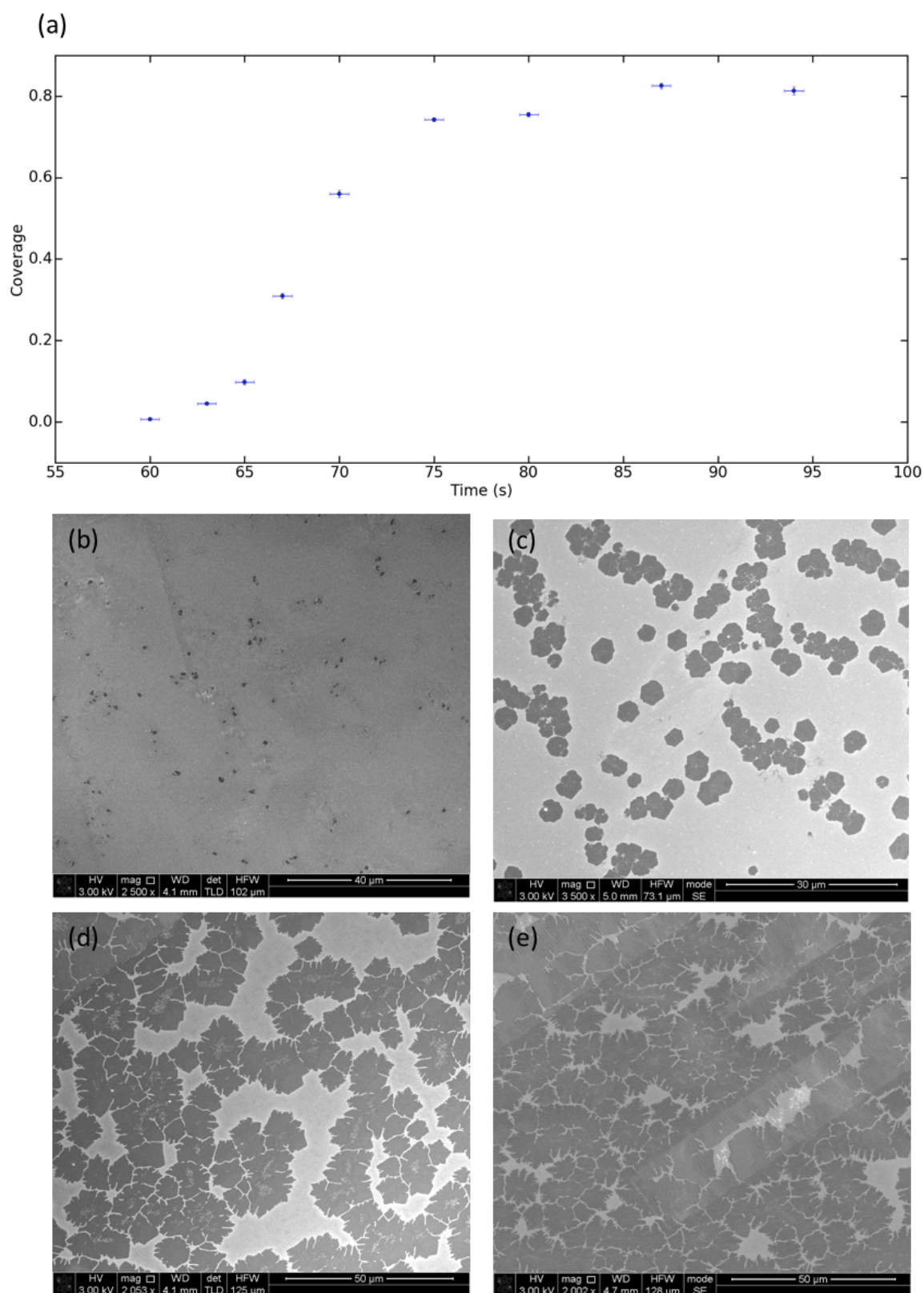


Figure 4.3: Graphene coverage evolution with time, (a), and SEM micrographs of graphene domains grown under a stream of  $\text{CH}_4$  for 60 s, (b), 67 s, (c), 80 s, (d), and 87 s, (e).

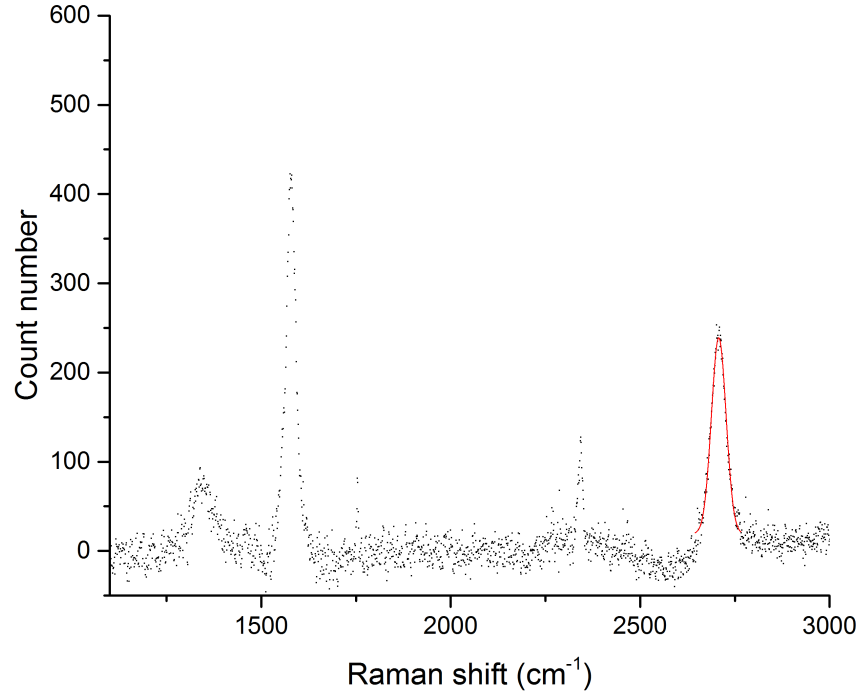


Figure 4.4: Raman spectrum of as-grown graphene. The red lines shows a Lorentzian fit to the  $2D$  peak.

Section 3.2; however, the samples produced at  $\text{CH}_4$  flow times of  $t < 65$  s did not show any Raman peaks associated with graphene due to the very small sizes of graphene islands and the difficulty of positioning them in the probed volume. A representative Raman spectrum of a graphene sample grown at a longer time  $t = 65$  s is shown in Fig. 4.4. Generally, the spectra contain three graphene-related peaks:  $D$ ,  $G$  and  $2D$  at the expected positions of  $1349 \pm 2 \text{ cm}^{-1}$ ,  $1585 \pm 1 \text{ cm}^{-1}$  and  $2717 \pm 2 \text{ cm}^{-1}$ . As discussed in Section 2.1.4, the relative intensities of these bands can give information on the defect density and the thickness of a sample; therefore, the peak intensity ratios  $I_D/I_G$  and  $I_{2D}/I_G$  were plotted as a function of growth time, as shown in Fig. 4.5. The  $I_D/I_G$  ratio, which is often used to quantify the defect density in a graphene sheet due to the nature of the defect-induced  $D$  band, is fairly low and seems to follow a slightly decreasing trend with growth time. Intuitively, the defect density of the samples should increase with an increasing coverage as a result of the formation of grain boundaries and developing dendritic island shape, which introduces more edge structures. Nonetheless, it has been shown that the relationship between the  $I_D/I_G$  ratio and the average distance between the defects,  $L_D$ , is generally non-linear and can increase with increasing  $L_D$  up to 4 nm [72]. The relationship between the  $I_{2D}/I_G$  ratio and the growth time does

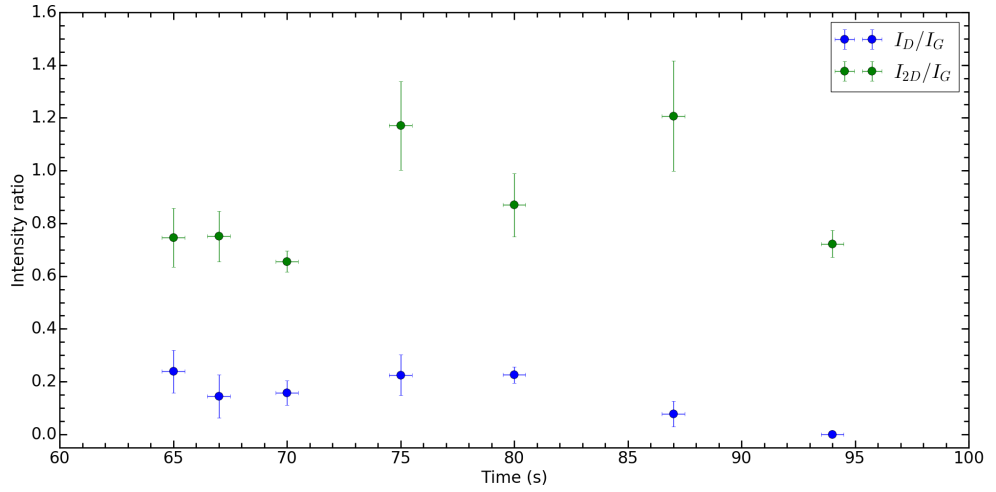


Figure 4.5: Evolution of intensity ratios  $I_D/I_G$  and  $I_{2D}/I_G$ .

not show any variation to within experimental error. Often, the  $I_{2D}/I_G$  ratio is used in the literature as an indicator of the number of graphene layers [71]. It is typically considered that monolayer graphene has a  $2D$  band, the intensity of which is at least twice as high as the intensity of the  $G$  band. However, this has been shown not to be a reliable way to define the thickness of a sample due to the sensitivity of the  $2D$  band intensity to defects [107] and doping [108]. Here, the shape of the  $2D$  peak is a more reliable means to determine its thickness: the  $2D$  line is symmetric for monolayer graphene and can be fitted with a single, relatively narrow Lorentzian, while the peak is asymmetric for multilayer graphene and shows multiple Lorentzian features, as shown in Fig. 4.6 [71]. Turbostratic graphene, i.e. multilayer graphene with relative interlayer rotations and therefore decoupled electronic states between the layers, also has a symmetric  $2D$  peak, but one with a very large linewidth [109]. Despite the low  $I_{2D}/I_G$  ratio of the graphene samples produced in this work, the  $2D$  peak can be normally fitted with a single Lorentzian with FWHM of approximately  $35 \text{ cm}^{-1}$ , as shown in Fig. 4.4. Hence, it is reasonable to infer that the samples consist of predominantly single layer graphene, which is also confirmed by the high island transparency and low density of secondary layers (which appear darker) seen in SEM micrographs.

### 4.3.2 The kinetics of graphene growth

As mentioned in Section 1.4, several attempts have been made to describe the kinetics of graphene growth by CVD. The suggestion to use a modified JMAK model made by Kim *et*

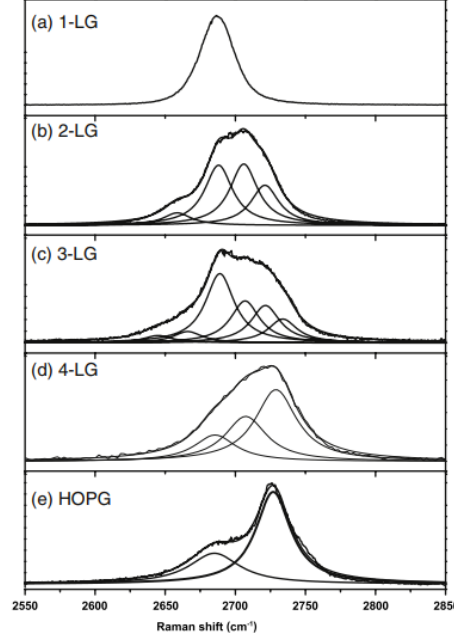


Figure 4.6: The shapes of Raman 2D band of 1-4 layer graphene (LG), (a)-(d) respectively, and HOPG, (e) [71].

*al.*, stemmed from their derivation of a growth model defined by the equation

$$A_G = A_{sat} \left( \frac{\exp(k_1 \rho_G \sqrt{A_{sat}} (t - t_0)) + 1}{\exp(k_1 \rho_G \sqrt{A_{sat}} (t - t_0)) - 1} \right)^2, \quad (4.3.1)$$

where  $A_G$  is the total area of the graphene islands at time  $t$ ,  $A_{sat}$  is the saturation area (i.e. the coverage at  $t \rightarrow \infty$ ),  $k_1$  is a rate parameter related to the number of carbon atoms attaching to the edge of a graphene domain,  $\rho_G$  is the atomic area density of graphene,  $0.382 \text{ \AA}^{-2}$ ,  $t$  is time and  $t_0$  is time lag at which observable nuclei start to form [51]. The key assumptions underpinning the model include complete dehydrogenation of  $\text{CH}_4$  on the Cu surface, island nucleation when the carbon monomer concentration,  $c_{cu}$ , reaches a critical supersaturation level,  $c_{nuc}$ , island growth in a carbon attachment-limited regime, which proceeds until  $c_{cu}$  reaches the equilibrium level,  $c_{eq}$ , and termination of  $\text{CH}_4$  dissociation after nucleation takes place [51]. However, the functional form of the model, as presented in the paper [51] and equation 4.3.1, has an unphysical asymptotic behaviour, i.e.  $\lim_{t \rightarrow t_0} A_G = \infty$ , implying that graphene coverage would be of infinite size at  $t = t_0$ , and would decrease as  $t \rightarrow \infty$  for  $t > t_0$ . A general curve representing the equation 4.3.1 is depicted in Fig. 4.7(a). Its inverse,

$$A_G = A_{sat} \left( \frac{\exp(k_1 \rho_G \sqrt{A_{sat}} (t - t_0)) - 1}{\exp(k_1 \rho_G \sqrt{A_{sat}} (t - t_0)) + 1} \right)^2, \quad (4.3.2)$$

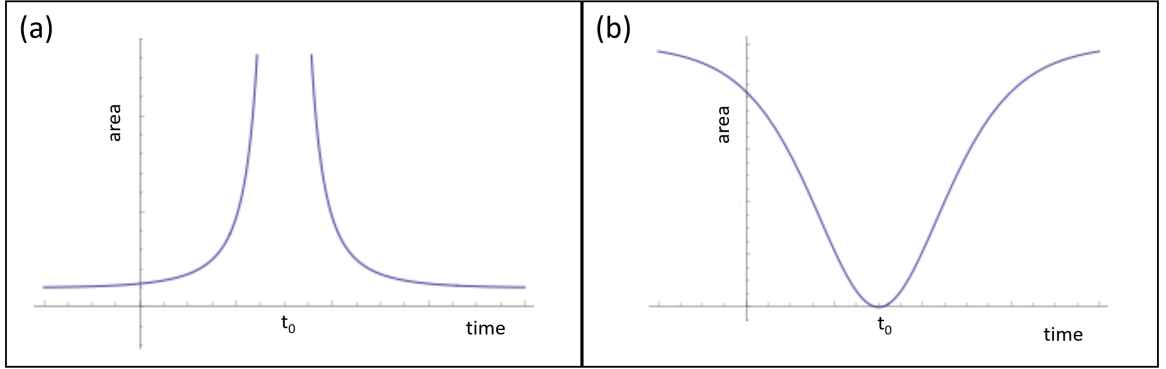


Figure 4.7: Graphical representation of equation 4.3.1, (a), and its inverse, (b).

on the other hand, produces a reasonable prediction of the area evolution for  $t > t_0$ , as shown in Fig. 4.7(b), which also agrees with a general lineshape of the standard JMAK model

$$f_V = 1 - \exp(-kt^n), \quad (4.3.3)$$

where  $f_V$  is the fraction of transformed volume,  $k$  is the reaction rate constant,  $t$  is time and  $n$  is the Avrami exponent [53]. Therefore, it is clear that equation 4.3.1, as presented by Kim *et al.*, contains a typographical error, with its inverse, equation 4.3.2, being the correct form as can be seen by following the derivation of Kim *et al.* Furthermore, a careful inspection of the evolution of graphene coverage and the fitting of the modified JMAK model to the data, as shown in Fig. 1.6, suggests that the fitting has no degrees of freedom (a four-parameter function was fitted to four data points) and also the plot indicates a negative value for the time lag,  $t_0$ . As the only fitting parameter value specified in the publication is for the Avrami exponent,  $n = 1.1 \pm 0.5$  [51], an independent fitting to the data presented by Kim *et al.* for growth at a temperature of 720° C was carried out, giving the remaining parameter values:  $A_{sat} = 0.53$ ,  $k = -0.001 \text{ s}^{-1}$  and  $t_0 = -132.85 \text{ s}$ . Evidently, the negative value obtained for  $t_0$  is incompatible with its definition: a finite graphene coverage at negative  $t > t_0$  implies that the domain nucleation starts before the system is exposed to  $\text{CH}_4$ . Therefore, the application of the JMAK model to describe the graphene growth pattern observed by Kim *et al.* cannot be correct.

Nonetheless, the model was fitted to the coverage data of the samples grown in this work, setting the upper bound for the time lag to be 60 s. The resulting best fit has parameter values of  $A_{sat} = 0.82$ ,  $k = -0.012 \text{ s}^{-1}$ ,  $t_0 = 60 \text{ s}$  and  $n = 1.9$ , and is shown in Fig. 4.8. The curve seems to reflect a very similar growth behaviour; however, the  $\chi^2$  value of 133 for the fitting is very high, which may be partially caused by the small errors in coverage resulting

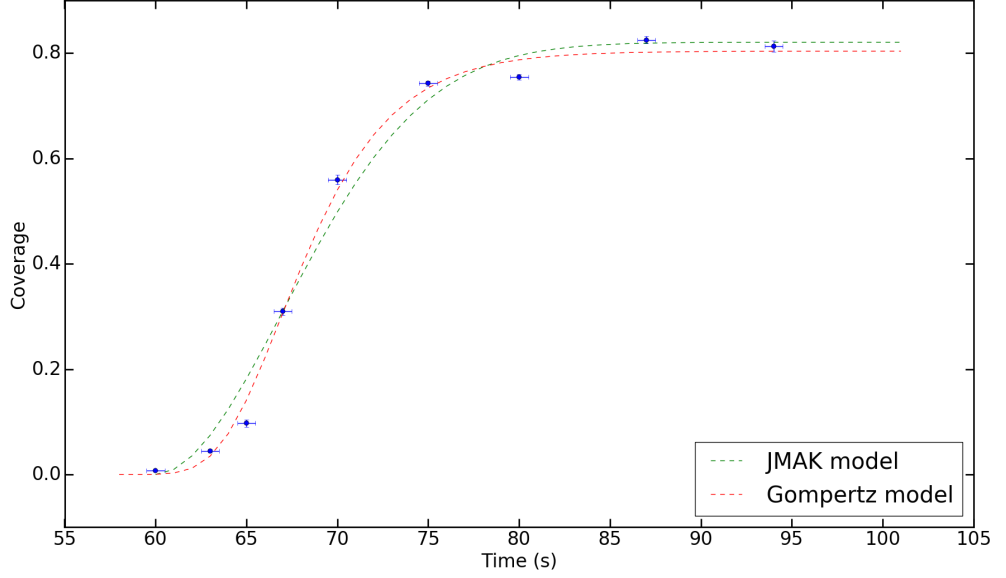


Figure 4.8: Modified JMAK (green) and modified Gompertz (red) model fitting to the coverage data obtained from the as-grown samples.

from only one sample (but many images) being analysed for each  $\text{CH}_4$  flow time. Therefore, in order to test the applicability of the JMAK model, it is useful to look at the constancy of the Avrami exponent,  $n$ .

Generally, the Avrami exponent can be expressed as

$$n = N_{dim}g + B, \quad (4.3.4)$$

where  $N_{dim}$  is the dimensionality of the growth,  $g$  is a parameter reflecting the type of growth (linear or parabolic) and  $B$  defines the nucleation mode (site-saturated or constant nucleation) [110]. An important aspect of the JMAK model is that the Avrami exponent has to stay constant over the entire process of transformation. Hence, a linearised version of the growth model should produce a straight line, the slope of which would give the value for the Avrami exponent. A linearised version for the modified JMAK model of Kim *et al.* can be expressed by

$$\ln \left( -\ln \left( 1 - \frac{A}{A_{sat}} \right) \right) = \ln(k') + n \ln(t - t_0), \quad (4.3.5)$$

where the  $k$  parameter in the modified JMAK model was defined for convenience as  $-k'$ , in accordance to the fitting results and the standard JMAK model. Linearisation of the growth data measured in this work is shown in Fig. 4.9. where  $A_{sat} = 0.83$  and  $t_0 = 59$  s were chosen in order to avoid undefined values at certain coverages and nucleation time. Clearly, the

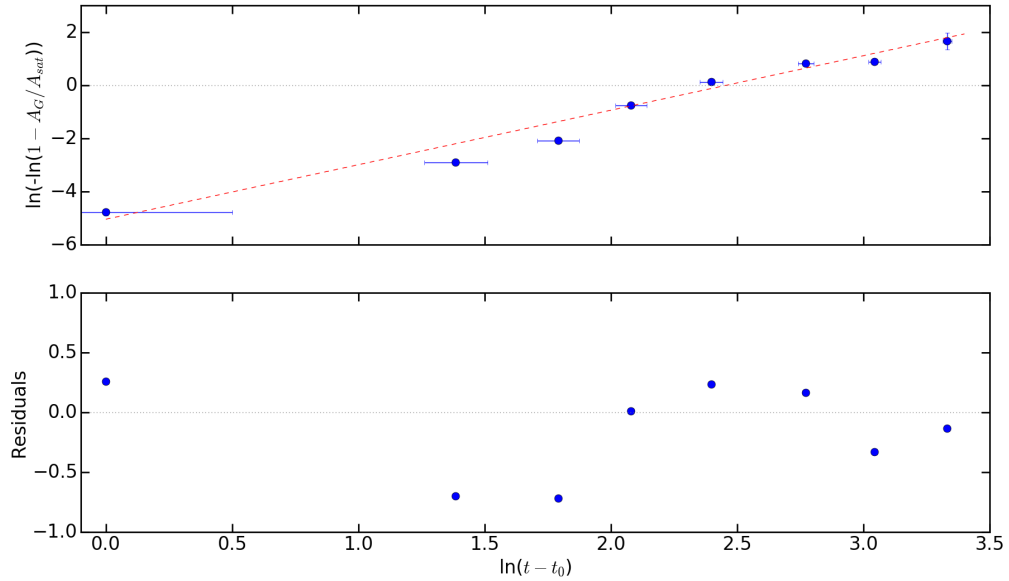


Figure 4.9: Linearised JMAK model for graphene growth. The red line represent the best linear fit.

Avrami coefficient is non-linear, as suggested by non-randomly scattered residuals. This is further evidence to conclude that a modified JMAK model is not a reasonable representation of graphene growth by CVD on Cu using  $\text{CH}_4$  as a precursor.

Another widely discussed model used to describe graphene coverage evolution on Cu is a modified Gompertz model, proposed by Celebi *et al.* [57] The model is based on a substrate surface mediated catalytic decomposition of ethylene into a mixture of carbon dimers, monomers and intermediate species, which nucleate when their concentration reaches a critical supersaturation level. As opposed to the JMAK model, Gompertzian kinetics defines the growth of graphene islands supported by a continuous supply of film forming species until either complete or saturated substrate coverage is reached. As shown in Fig. 1.7, Celebi *et al.* plotted the model defined by equation 1.4.2 to two data sets consisting of four data points each, which gives only one degree of freedom, and therefore makes the fitting unreliable. Celebi *et al.* also define graphene growth in terms area evolution of individual domains, which, in the case of approximately constant nucleation density and a minimal number of secondary layers, can be equated to overall graphene coverage evolution on a substrate. Therefore, equation 1.4.2 was fitted to the growth data obtained in this work and the resulting best fit is depicted in Fig. 4.8 in red. The modified Gompertz model seems to reflect the observed growth pattern slightly better than the JMAK model, and has the parameter values

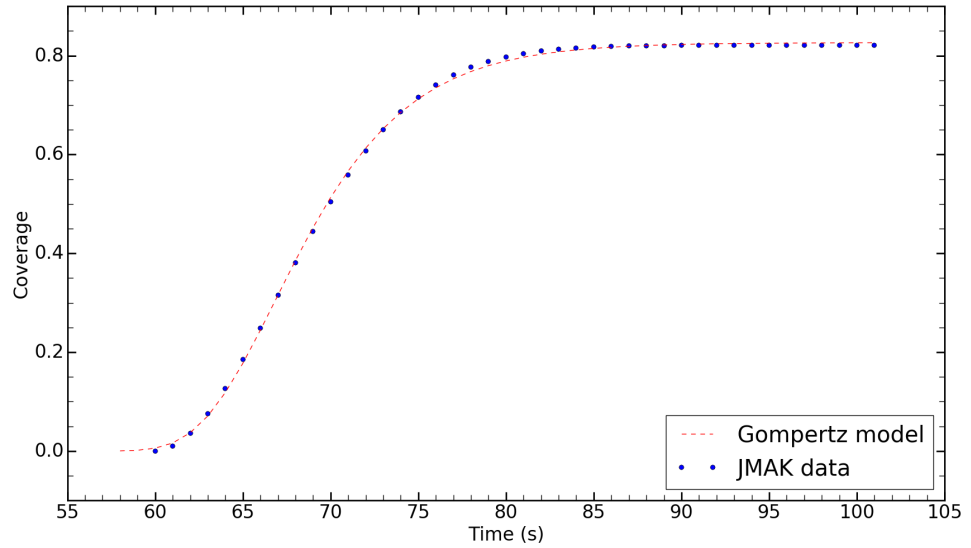


Figure 4.10: Gompertz model fitting to the growth data defined by the JMAK model.

of  $A_{max} = 0.80$ ,  $\mu_m = 0.087 \text{ s}^{-1}$  and  $\lambda = 63.5 \text{ s}$ . Nonetheless, the fitting has a high  $\chi^2$  value of 97, at least partially caused by the small errors in coverage. Furthermore, it can be seen that the model produces a very similar curve to the JMAK model. Hence, in order to study similarities between predicted growth kinetics of the models, a data set consisting of 42 points defined by the modified JMAK curve was created and fitted with the modified Gompertz model, as shown in Fig. 4.10. The data-defining parameters were set to be the same as the ones obtained from the fitting of the JMAK model to the coverage data of as-grown graphene samples. Evidently, the Gompertz model fits the JMAK-defined growth data (and vice versa) fairly well, which suggests that the models may be indistinguishable based on the functional form of transformation alone. In fact, potentially a number of sigmoidal functions could be successfully fitted to sigmoidal growth data; however, their applicability should be determined on how well the set of fundamental assumptions defining each model reflects the experimental conditions for graphene growth and the physical reasonableness of the resulting fit parameters. From this perspective, the modified Gompertz model provides a reasonable description of the CVD graphene growth mechanism and the evolution of global coverage; however, it does not account for the coverage differences observed at a lower growth temperature, which are described in detail in Section 4.3.3.

### 4.3.3 Influence of copper morphology on the graphene growth

As briefly outlined in Section 4.2, SEM characterisation of as-grown graphene samples prepared at 1065°C revealed a number of Cu-grain-dependent differences in graphene growth, which are depicted in Fig. 4.2. Clearly, to the left side of the Cu grain boundary, graphene islands seem to nucleate at lower densities and cluster into similarly aligned elongated structures, as opposed to the ones on the right, which nucleate sporadically and fairly densely. In order to explore the differences in growth and its consistency further, several new samples were prepared following the standard sample cleaning and growth procedure specified in Section 4.2, but at a lower growth temperature of 1025°C. The SEM characterisation of islands showed a more prominent disparity in their morphology than previously observed, as depicted in Fig. 4.11(a), (b) and (c).

Evidently, inhomogeneous nucleation and anisotropic growth of graphene island chains, which are confined to particular Cu grains, are influenced by morphological substrate properties. A careful inspection of the growth direction and chain curvature at high magnifications suggests that these islands grow along Cu steps (or step bunches) as shown in Fig. 4.12. However, due to a generally stepped structure of the entire Cu surface, it is not clear why such growth is observed only on certain grains. Therefore, in order to determine the origin of island morphological differences and also quantify graphene coverage on different Cu grains, the samples grown at 1065°C and 1025°C, were probed by SEM in the EBSD mode to reveal the surface structure and crystallographic orientation of the underlying Cu grains. An example of a secondary electron image of Cu surface and a corresponding EBSD map is shown in Fig. 4.13(a) and (b) respectively.

Clearly, anisotropic island growth occurs on very rough grains, step bunches of which are visible in the forward scattered electron image of the Cu surface, while the grains supporting isotropic island nucleation and growth are smooth. As the sample growth temperature increases from 1025°C to 1065°C, the surface roughness reduces and results in less prominent differences in island growth. Orientation analysis shows that the rougher grains have orientations of (111) or very similar, such as (223) or (233).

Anisotropic growth of graphene ribbons along the steps of a single crystal Cu(111) surface has been previously observed in LPCVD [111], as shown in Fig 4.14(a) and (b). Hayashi *et al.* proposed that graphene ribbon formation results from Cu evaporation and step bunching at lower pressures, i.e. it is thought that nucleated graphene islands stabilise the Cu surface underneath them and therefore pin Cu steps, which otherwise "move" due to diffusion and

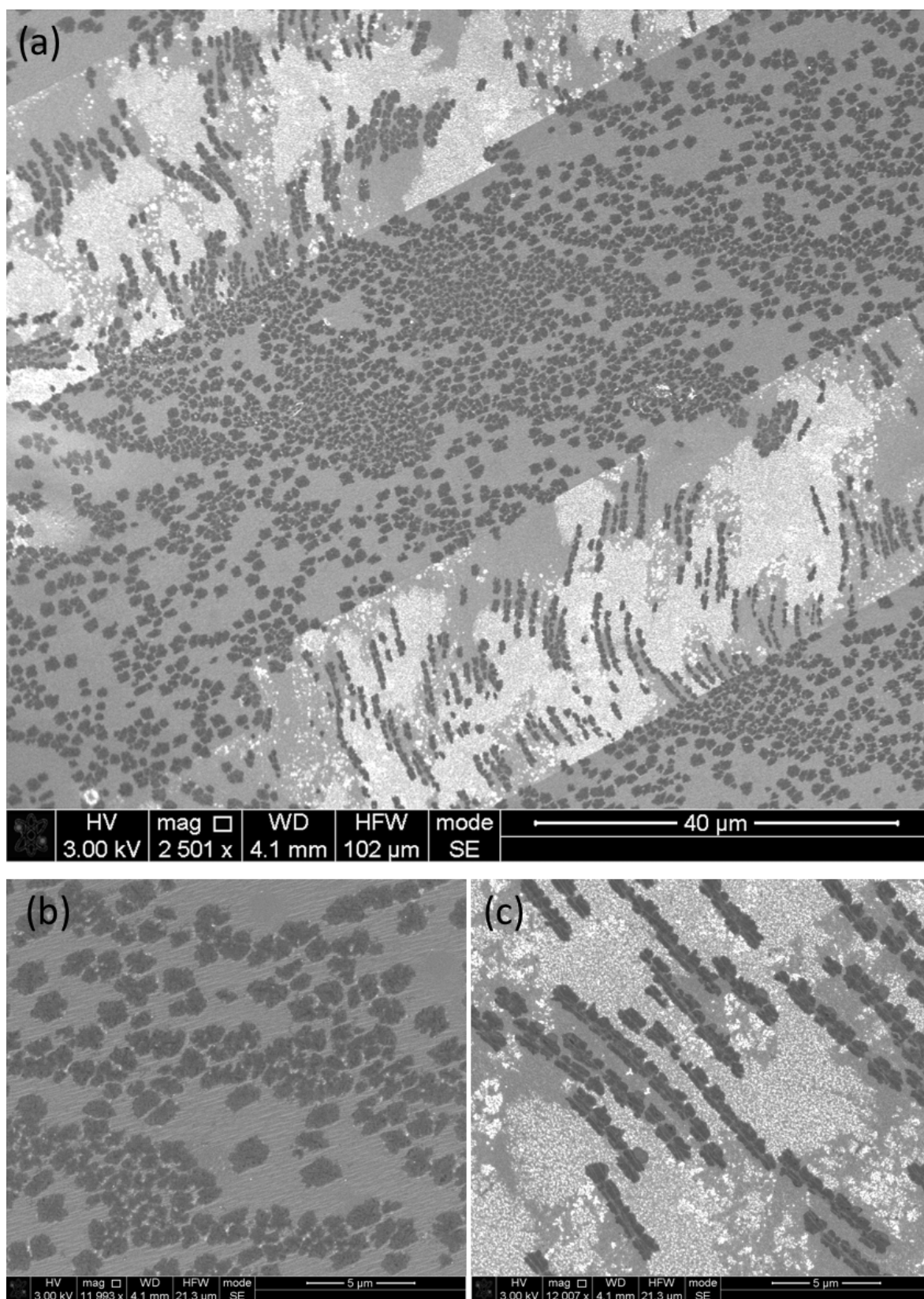


Figure 4.11: Morphological differences of graphene islands grown on different Cu grains.

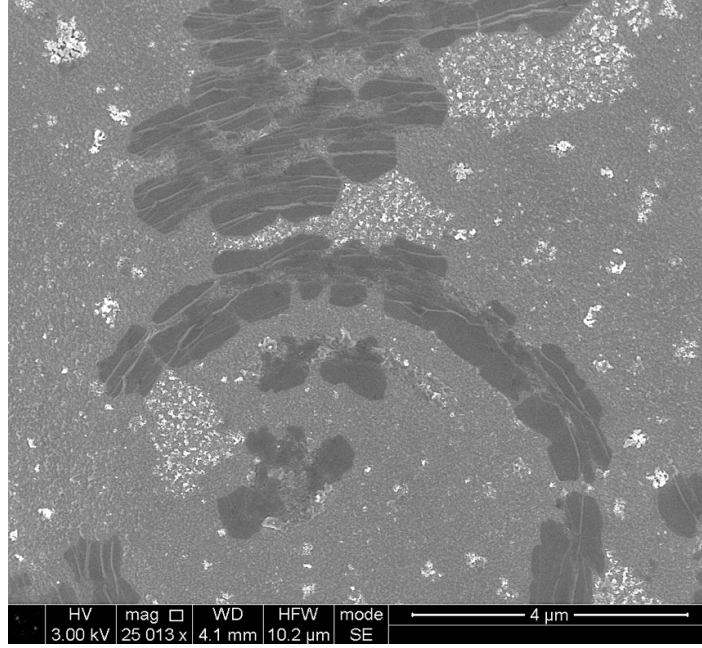


Figure 4.12: Graphene island nucleation along Cu steps.

evaporation of Cu atoms (Fig. 4.15). At the same time, free carbon species adsorbed on the bunched steps are integrated into the graphene islands along the steps, resulting in a ribbon growth [111]. Hayashi *et al.* also claim that this growth behaviour should not be observed in APCVD due to low Cu evaporation rates, even distribution of steps and relatively narrow terraces, over which graphene islands can connect to the neighbours [111].

In APCVD, higher Cu evaporation rates are achieved at high temperature growth; however, growth anisotropy on as-grown samples is more prominent at lower temperatures, which rules out passivation of substrate under graphene islands and step bunching due to evaporation. Therefore, further studies are needed in order to determine the origin of amplified surface roughness on (111) and similar grains in comparison to the rest of the substrate at lower temperatures.

Further EBSD analysis showed that copper substrates were mostly composed of grains, with surfaces defined by high Miller indices. Such faces are thought to consist of terraces of atoms that are separated by a series of atomic-height steps, which can also include kinks [112]. According to Van Hove *et al.* [112], a surface of an arbitrary orientation, expressed by an irreducible Miller index vector  $\vec{u}_0 = (h_0k_0l_0)$ , can be decomposed into three microfacets with linearly independent Miller indices,  $\vec{u}_1$ ,  $\vec{u}_2$  and  $\vec{u}_3$ , i.e.

$$\vec{u}_0 = a_1\vec{u}_1 + a_2\vec{u}_2 + a_3\vec{u}_3, \quad (4.3.6)$$

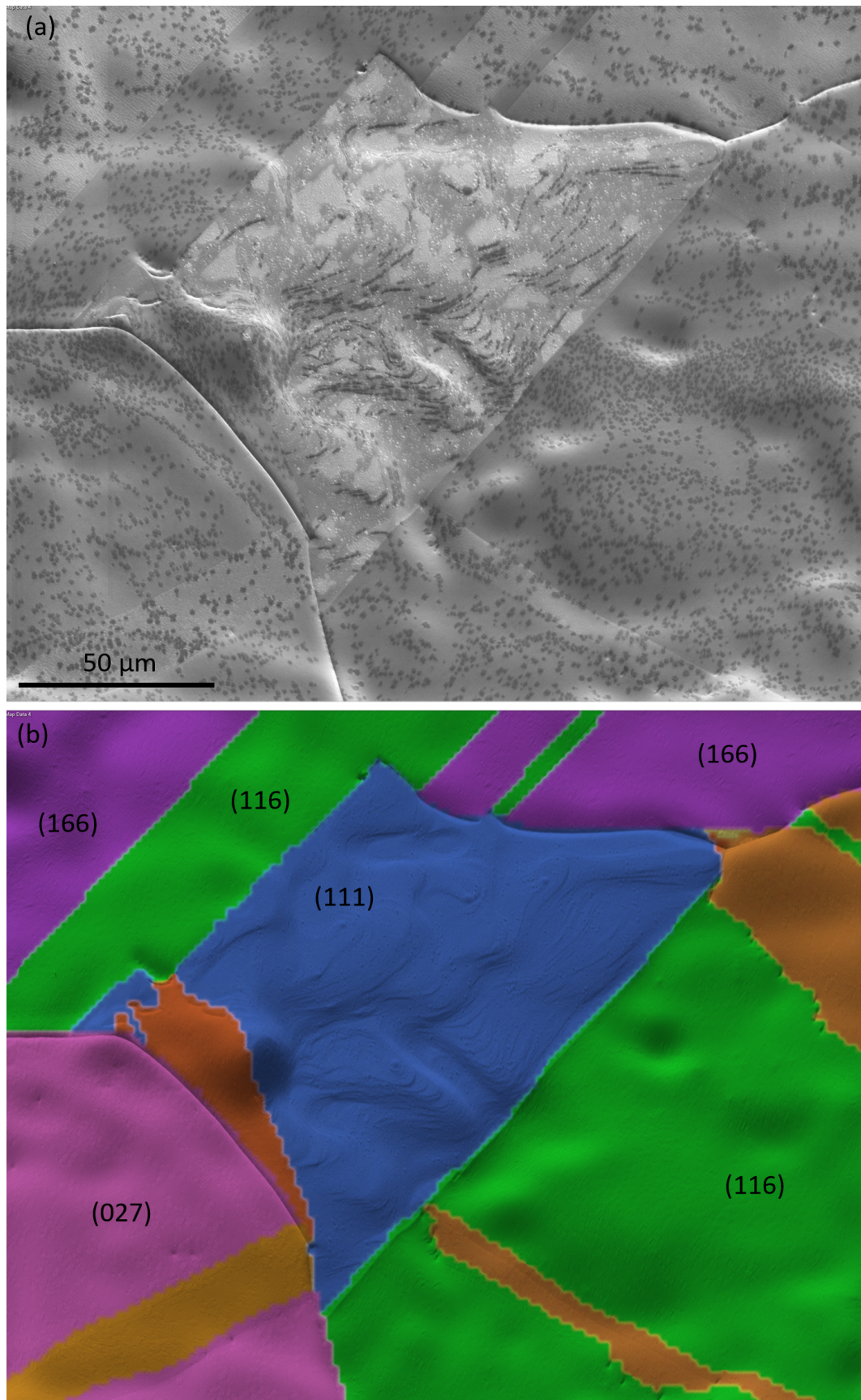


Figure 4.13: Secondary electron image of Cu surface, (a), and an EBSD map superimposed with a forward scattered electron image of the same area, (b).

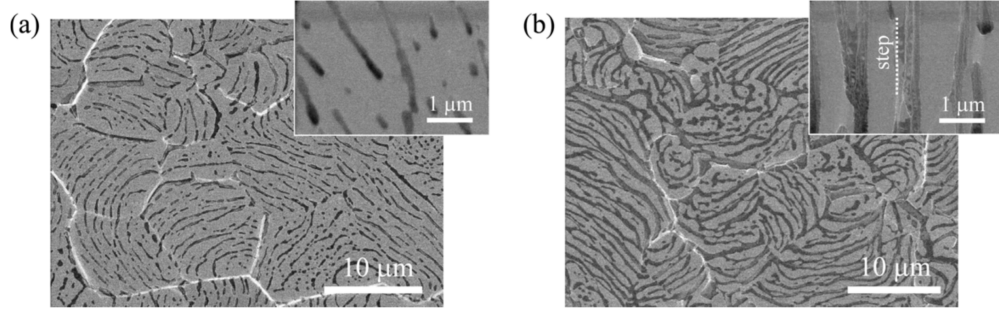


Figure 4.14: SEM images of anisotropic graphene growth along the steps of Cu(111) surface at  $\text{CH}_4$  exposure times of 20 min, (a), and 65 min, (b) [111].

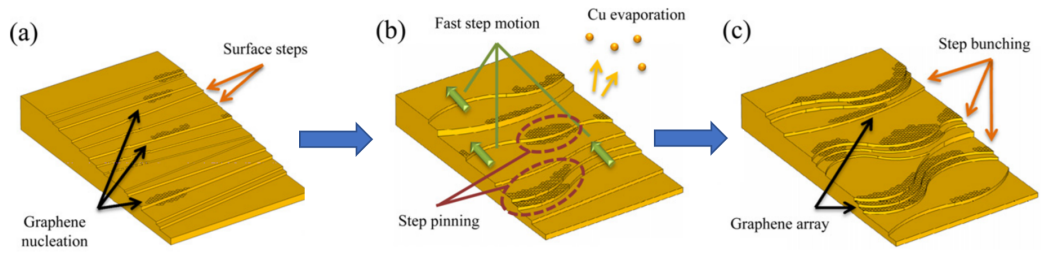


Figure 4.15: Graphene ribbon formation on Cu during LPCVD: graphene nucleation at surface steps, (a), fast step motion due to Cu evaporation and step pinning under graphene islands, (b), and step bunching, (c). Image adapted from [111].

where  $a_1$ ,  $a_2$  and  $a_3$  are the decomposition coefficients, which are related to the number of unit cells  $n_i^{\text{uc}}$  in each microfacet:

$$n_0^{\text{uc}} : n_1^{\text{uc}} : n_2^{\text{uc}} : n_3^{\text{uc}} = p_0 : a_1 p_1 : a_2 p_2 : a_3 p_3, \quad (4.3.7)$$

where, for a crystal of fcc symmetry like Cu,

$$p_i = \begin{cases} 2 & \text{if } h_i, k_i, l_i \text{ not all odd,} \\ 4 & \text{if } h_i, k_i, l_i \text{ all odd.} \end{cases} \quad (4.3.8)$$

Thus, high index surface planes can be decomposed into a combination of (111), (110) and (100) planes, weighted by the number of unit cells in each microfacet. As the (110) plane in fcc materials is not close-packed, Van Hove *et al.* suggest decomposing a high index facet into (111),  $(11\bar{1})$  and (100) microfacets instead; however, the former combination was chosen as it represents low index faces in fcc materials, which are also used in industrial production of Cu foils.

The resulting substrate grain orientation-dependent coverage data for the samples grown

at 1065°C (CH<sub>4</sub> exposure of 80 s) and 1025°C (CH<sub>4</sub> exposure of 67 s) is represented in Fig. 4.16(a), (b), (c) and Fig. 4.17(a), (b), (c) respectively. The results show that at high temperature, i.e. 1065 °C, the coverage of graphene islands is independent of increasing fractions of (100), (110) or (111), which could be linked to increased surface uniformity during graphene growth at temperatures close to the Cu melting point. Nonetheless, a quite large coverage scattering is seen on certain orientations. At lower temperatures, on the other hand, the coverage increases with increasing fraction of (100), and reduces with increasing fraction of (111) surface. The differences at lower temperatures might be caused by different CH<sub>4</sub> dissociation energies on various Cu faces, as DFT calculations have showed that for fcc metal substrates the (111) surface is less active than the (100) surface [56]. At higher growth temperatures, the Cu grains should become more structurally uniform producing very similar graphene coverages, which goes in line with the data obtained.

#### 4.4 Summary

The data obtained in this work shows that as-grown graphene consisted predominantly of monolayer islands, the coverage of which evolved in a sigmoidal manner. It was shown that the modified JMAK model could not be used to describe graphene growth by CVD and the issues associated with the application of the modified Gompertz model were outlined. An EBSD analysis of Cu surface texture showed that rough copper grains of orientations similar to (111) supported anisotropic growth of graphene island chains with lower nucleation density and coverage at lower growth temperature.

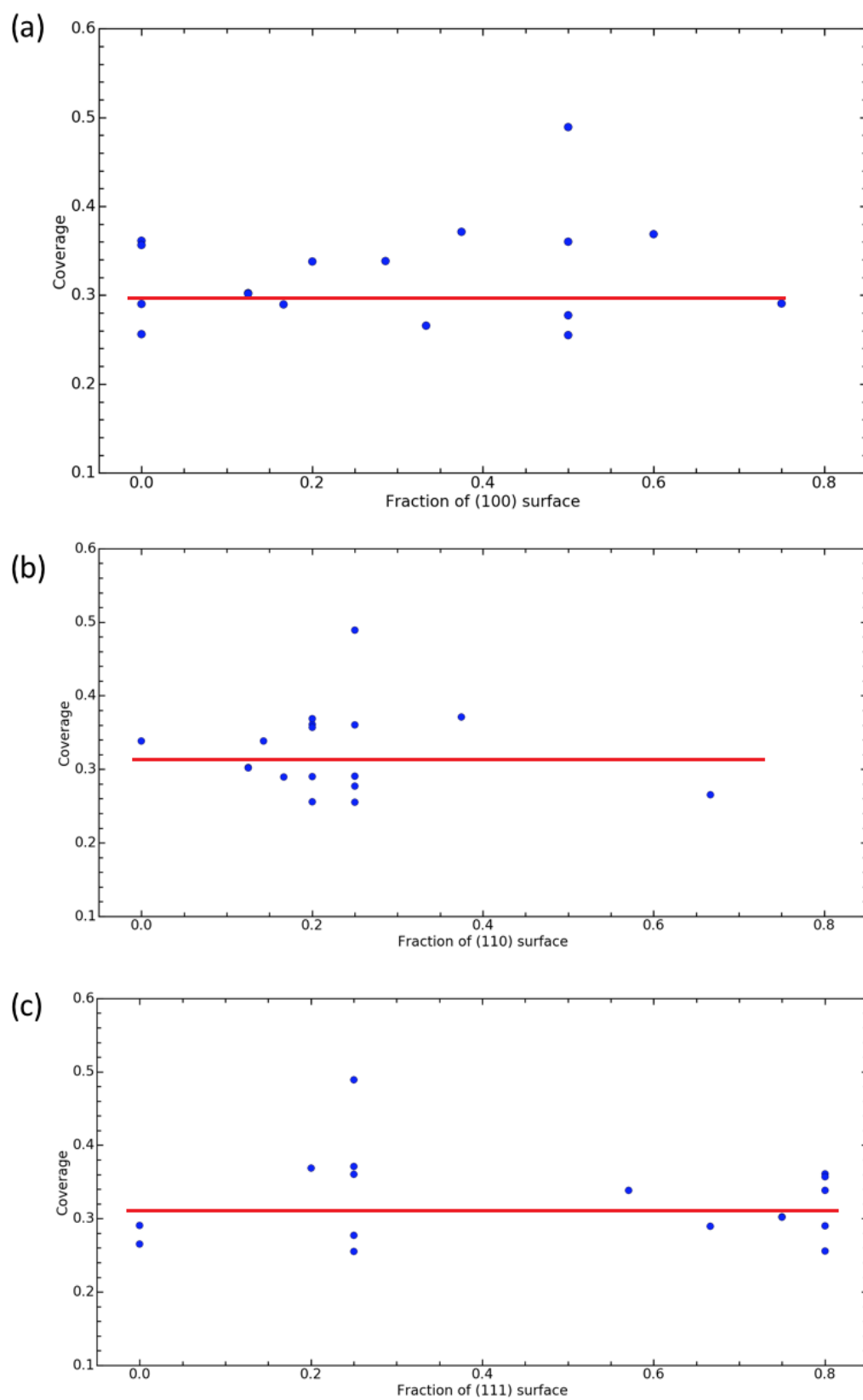


Figure 4.16: Graphene coverage of a sample grown at  $1065^{\circ}\text{C}$  with respect to a fraction of (100), (110) and (111) surfaces that high Miller index grains are composed of, (a), (b) and (c) respectively. Lines are a guide to the eye.

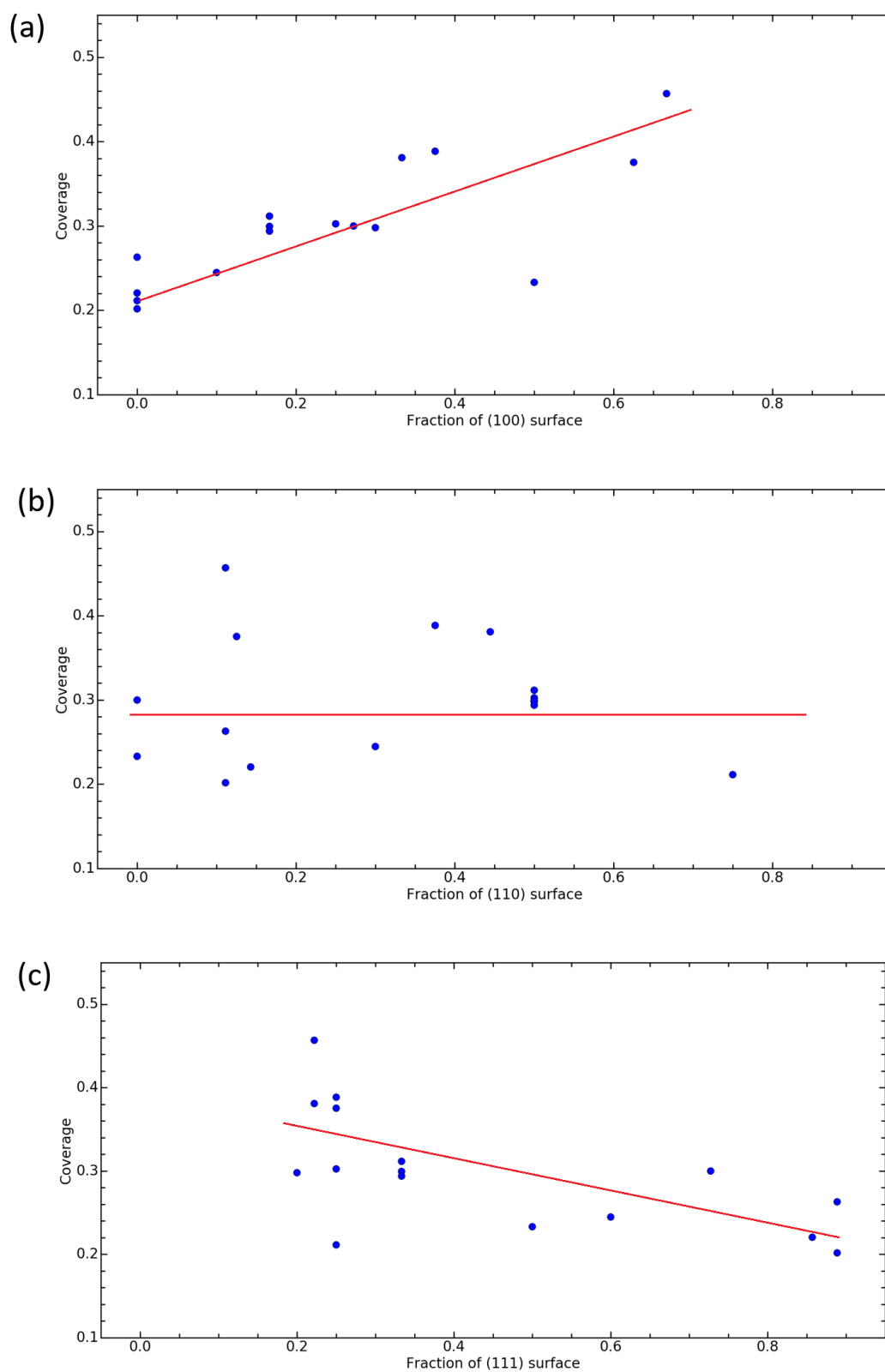


Figure 4.17: Graphene coverage of a sample grown at  $1025^{\circ}\text{C}$  with respect to a fraction of (100), (110) and (111) surfaces that high Miller index grains are composed of, (a), (b) and (c) respectively. Lines are a guide to the eye.

## Chapter 5

# Summary and further work

### 5.1 Summary

Graphene has emerged as a very interesting material with an exceptional electronic structure, leading to potential applications in a variety of fields such as flexible electronics, energy storage devices and sensors. As discussed in Chapter 1, graphene can be produced from graphite by a variety of exfoliation techniques or synthesised from carbonaceous species by CVD and MBE. In this work, graphene samples were produced in a hot-wall atmospheric pressure CVD system on polycrystalline Cu foils using  $\text{CH}_4$  as a precursor. The growth was carried out at  $1065^\circ\text{C}$  and  $1025^\circ\text{C}$  under a mixed precursor and 5%  $\text{H}_2/\text{Ar}$  carrier gas flow of 1 sccm and 300 sccm respectively. The quality of as-grown graphene samples was determined using Raman spectroscopy and SEM. Despite having a fairly low  $I_{2\text{D}}/I_{\text{G}}$  intensity ratio, the samples consisted of predominantly monolayer graphene and exhibited a relatively narrow  $2\text{D}$  peak, which could be fitted with a single Lorentzian.

A further study of graphene growth kinetics in relation to two kinetic models previously applied in the literature, i.e. modified JMAK and modified Gompertz models, revealed a sigmoidal evolution of graphene coverage as a function of a precursor flow time. Linearisation and fitting of the modified JMAK model to the growth data showed that the model was not suitable to describe graphene growth due to non-constant Avrami exponent and certain model assumptions on the continuity of precursor dehydrogenation after island nucleation and the composition of film-forming species, which contradicted theoretical calculations and the physical nature of CVD process. The modified Gompertz model, on the other hand, was built on reasonable assumptions about graphene growth and provided a good fit to the data.

SEM analysis of the samples also showed selective graphene island nucleation and anisotropic growth on certain Cu faces. Morphological differences between the domains were amplified at a lower growth temperature of 1025°C, where a number of Cu grains supported the formation of island chains at a lower nucleation density in comparison to the rest of the sample. An EBSD analysis of Cu surface texture revealed that the chains of graphene islands grew along the step bunches of very rough grains with orientations close to (111), while sporadic and dense nucleation was observed on smooth grains. Also, high Miller index Cu faces were decomposed into a combination of (111), (110) and (100) microfacets representing grain structure in terms terraces, steps and kinks. This allowed graphene coverage to be compared according to the fraction of different microfacets constituting a grain, with the results showing approximately constant graphene coverage on Cu grains after the growth at 1065°C but a decreasing trend with an increasing fraction of (111) terraces after growth at 1025°C.

## 5.2 Further work

As mentioned in Chapter 4, even at high growth temperature of 1065°C, graphene islands tended to nucleate at very high densities, which limited the lateral growth of islands and introduced many of grain boundaries within the domains when islands merged. Therefore, it would be useful to look into a number of different substrate cleaning procedures, test hydrogen plasma etching, different types of acid or surface polishing techniques. It would also be helpful to reduce a precursor partial pressure during growth; however, care must be taken if it is done by increasing the partial pressure of the carrier gas due to a risk of a transition from a laminar gas flow regime to a turbulent regime, which is unwanted do to possible inconsistencies in precursor adsorption and other stages of graphene growth.

A reduced and quantifiable nucleation density of graphene islands over prolonged intervals of growth time could also be used to explain growth differences between certain Cu grains: a measurement of a growth rate over a number of temperatures could give an insight into differences in the activation energies on different grains and therefore growth-limiting steps could be deduced.

# Bibliography

- [1] P R Wallace. The band theory of graphite. *Physical Review*, 71(9):622, 1947.
- [2] N D Mermin. Crystalline order in two dimensions. *Physical Review*, 176(1):250, 1968.
- [3] K S Novoselov, A K Geim, S V Morozov, D Jiang, Y Zhang, S V Dubonos, I V Grigorieva, and A A Firsov. Electric field effect in atomically thin carbon films. *Science*, 306(5696):666–669, 2004.
- [4] A K Geim and K S Novoselov. The rise of graphene. *Nature Materials*, 6(3):183–191, 2007.
- [5] W Choi, N Choudhary, G H Han, J Park, D Akinwande, and Y H Lee. Recent development of two-dimensional transition metal dichalcogenides and their applications. *Materials Today*, 2017.
- [6] M E Dávila, L Xian, S Cahangirov, A Rubio, and G Le Lay. Germanene: a novel two-dimensional germanium allotrope akin to graphene and silicene. *New Journal of Physics*, 16(9):095002, 2014.
- [7] C L Lin, R Arafune, K Kawahara, N Tsukahara, E Minamitani, Y Kim, N Takagi, and M Kawai. Structure of silicene grown on ag (111). *Applied Physics Express*, 5(4):045802, 2012.
- [8] A Khandelwal, K Mani, M H Karigerasi, and I Lahiri. Phosphorene—the two-dimensional black phosphorous: Properties, synthesis and applications. *Materials Science and Engineering: B*, 221:17–34, 2017.
- [9] H Zhu. *Graphene: Fabrication, Characterizations, Properties and Applications*. Academic Press, 2017.
- [10] W Choi and J Lee. *Graphene: Synthesis and Applications*. Nanomaterials and their Applications. CRC Press, 2016.

- 
- [11] J H Warner, F Schaffel, M Rummeli, and A Bachmatiuk. *Graphene: Fundamentals and emergent applications*. Elsevier Science, 2012.
- [12] H Aoki and M S Dresselhaus. *Physics of Graphene*. Springer Science & Business Media, 2013.
- [13] C Lee, X Wei, J W Kysar, and J Hone. Measurement of the elastic properties and intrinsic strength of monolayer graphene. *Science*, 321(5887):385–388, 2008.
- [14] H I Rasool, C Ophus, W S Klug, A Zettl, and J K Gimzewski. Measurement of the intrinsic strength of crystalline and polycrystalline graphene. *Nature Communications*, 4:2811, 2013.
- [15] Q X Pei, Y W Zhang, and V B Shenoy. A molecular dynamics study of the mechanical properties of hydrogen functionalized graphene. *Carbon*, 48(3):898–904, 2010.
- [16] A Zandiatashbar, G H Lee, S J An, S Lee, N Mathew, M Terrones, T Hayashi, C R Picu, J Hone, and N Koratkar. Effect of defects on the intrinsic strength and stiffness of graphene. *Nature communications*, 5:3186, 2014.
- [17] A Bellunato, H Arjmandi Tash, Y Cesa, and G F Schneider. Chemistry at the edge of graphene. *ChemPhysChem*, 17(6):785–801, 2016.
- [18] T Y Kim, C H Park, and N Marzari. The electronic thermal conductivity of graphene. *Nano letters*, 16(4):2439–2443, 2016.
- [19] T H Han, H Kim, S J Kwon, and T W Lee. Graphene-based flexible electronic devices. *Materials Science and Engineering: R: Reports*, 118:1–43, 2017.
- [20] J Heo, K E Byun, J Lee, H J Chung, S Jeon, S Park, and S Hwang. Graphene and thin-film semiconductor heterojunction transistors integrated on wafer scale for low-power electronics. *Nano letters*, 13(12):5967–5971, 2013.
- [21] D W Chang, H J Choi, A Filer, and J B Baek. Graphene in photovoltaic applications: organic photovoltaic cells (opvs) and dye-sensitized solar cells (dsscs). *Journal of Materials Chemistry A*, 2(31):12136–12149, 2014.
- [22] R Raccichini, A Varzi, S Passerini, and B Scrosati. The role of graphene for electrochemical energy storage. *Nature Materials*, 14(3):271, 2015.

- [23] C I L Justino, A R Gomes, A C Freitas, A C Duarte, and T A P Rocha-Santos. Graphene based sensors and biosensors. *TrAC Trends in Analytical Chemistry*, 91:53–66, 2017.
- [24] J Molina. Graphene-based fabrics and their applications: a review. *RSC Advances*, 6(72):68261–68291, 2016.
- [25] M Yi and Z Shen. A review on mechanical exfoliation for the scalable production of graphene. *Journal of Materials Chemistry A*, 3(22):11700–11715, 2015.
- [26] F Bonaccorso, A Lombardo, T Hasan, Z Sun, L Colombo, and A C Ferrari. Production and processing of graphene and 2d crystals. *Materials today*, 15(12):564–589, 2012.
- [27] H Zhu, Y Cao, J Zhang, W Zhang, Y Xu, J Guo, W Yang, and J Liu. One-step preparation of graphene nanosheets via ball milling of graphite and the application in lithium-ion batteries. *Journal of materials science*, 51(8):3675–3683, 2016.
- [28] V Nicolosi, M Chhowalla, M G Kanatzidis, M S Strano, and J N Coleman. Liquid exfoliation of layered materials. *Science*, 340(6139):1226419, 2013.
- [29] W K Park, Ye Yoon, Y H Song, S Y Choi, S Kim, Y Do, J Lee, H Park, D H Yoon, and W S Yang. High-efficiency exfoliation of large-area mono-layer graphene oxide with controlled dimension. *Scientific reports*, 7(1):16414, 2017.
- [30] T S Tran, S J Park, S S Yoo, T R Lee, and T Kim. High shear-induced exfoliation of graphite into high quality graphene by taylor–couette flow. *RSC Advances*, 6(15):12003–12008, 2016.
- [31] G R Kumar, K Jayasankar, S K Das, T Dash, A Dash, B K Jena, and B K Mishra. Shear-force-dominated dual-drive planetary ball milling for the scalable production of graphene and its electrocatalytic application with pd nanostructures. *RSC Advances*, 6(24):20067–20073, 2016.
- [32] X Fan, D W Chang, X Chen, J B Baek, and L Dai. Functionalized graphene nanoplatelets from ball milling for energy applications. *Current Opinion In Chemical Engineering*, 11:52–58, 2016.
- [33] C Teng, D Xie, J Wang, Z Yang, G Ren, and Y Zhu. Ultrahigh conductive graphene paper based on ball-milling exfoliated graphene. *Advanced Functional Materials*, 27(20), 2017.

- [34] M Cai, D Thorpe, D H Adamson, and H C Schniepp. Methods of graphite exfoliation. *Journal of Materials Chemistry*, 22(48):24992–25002, 2012.
- [35] C Zhang, W Lv, X Xie, D Tang, C Liu, and Q H Yang. Towards low temperature thermal exfoliation of graphite oxide for graphene production. *Carbon*, 62:11–24, 2013.
- [36] M Kruskopf, K Pierz, S Wundrack, R Stosch, T Dziomba, C C Kalmbach, A Müller, J Baringhaus, C Tegenkamp, F J Ahlers, et al. Epitaxial graphene on sic: modification of structural and electron transport properties by substrate pretreatment. *Journal of Physics: Condensed Matter*, 27(18):185303, 2015.
- [37] F Maeda and H Hibino. Thin graphitic structure formation on various substrates by gas-source molecular beam epitaxy using cracked ethanol. *Japanese Journal of Applied Physics*, 49(4S):04DH13, 2010.
- [38] M Y Lin, W C Guo, M H Wu, P Y Wang, T H Liu, C W Pao, C C Chang, S C Lee, and S Y Lin. Low-temperature grown graphene films by using molecular beam epitaxy. *Applied Physics Letters*, 101(22):221911, 2012.
- [39] T S Cheng, A Davies, A Summerfield, Y Cho, I Cebula, R J A Hill, C J Mellor, A N Khlobystov, T Taniguchi, K Watanabe, et al. High temperature mbe of graphene on sapphire and hexagonal boron nitride flakes on sapphire. *Journal of Vacuum Science & Technology B, Nanotechnology and Microelectronics: Materials, Processing, Measurement, and Phenomena*, 34(2):02L101, 2016.
- [40] A C Jones and M L Hitchman. *Chemical Vapour Deposition: Precursors, Processes and Applications*. Royal Society of Chemistry, 2009.
- [41] J Pang, A Bachmatiuk, I Ibrahim, L Fu, D Placha, G S Martynkova, B Trzebicka, T Gemming, J Eckert, and M H Rummeli. Cvd growth of 1d and 2d sp<sup>2</sup> carbon nanomaterials. *Journal of materials science*, 51(2):640–667, 2016.
- [42] C Wang, W Chen, C Han, G Wang, B Tang, C Tang, Y Wang, W Zou, X A Zhang, S Qin, et al. Growth of millimeter-size single crystal graphene on cu foils by circumfluence chemical vapor deposition. *Scientific reports*, 4:4537, 2014.
- [43] B Wang, M König, C J Bromley, B Yoon, M J Treanor, J A Garrido Torres, M Caffio, F Grillo, H Früchtl, N V Richardson, et al. Ethene to graphene: Surface catalyzed chemical pathways, intermediates, and assembly. *The Journal of Physical Chemistry C*, 121(17):9413–9423, 2017.

- [44] W Wu, Q Yu, P Peng, Z Liu, J Bao, and S S Pei. Control of thickness uniformity and grain size in graphene films for transparent conductive electrodes. *Nanotechnology*, 23(3):035603, 2011.
- [45] X Zhang, L Wang, J Xin, B I Yakobson, and F Ding. Role of hydrogen in graphene chemical vapor deposition growth on a copper surface. *Journal of the American Chemical Society*, 136(8):3040–3047, 2014.
- [46] I Vlassiouk, S Smirnov, M Regmi, S P Surwade, N Srivastava, R M Feenstra, G Eres, C Parish, N Lavrik, P Datskos, et al. Graphene nucleation density on copper: fundamental role of background pressure. *Journal of Physical Chemistry C*, 117(37):18919, 2013.
- [47] S Xing, W Wu, Y Wang, J Bao, and S S Pei. Kinetic study of graphene growth: temperature perspective on growth rate and film thickness by chemical vapor deposition. *Chemical Physics Letters*, 580:62–66, 2013.
- [48] Gi Duk Kwon, Eric Moyer, Yeo Jin Lee, Young Woo Kim, Seung Hyun Baik, and Didier Pribat. Influence of the copper substrate roughness on the electrical quality of graphene. *Materials Research Express*, 4(1):015604, 2017.
- [49] W Liu, H Li, C Xu, Y Khatami, and K Banerjee. Synthesis of high-quality monolayer and bilayer graphene on copper using chemical vapor deposition. *Carbon*, 49(13):4122–4130, 2011.
- [50] X Li, W Cai, L Colombo, and R S Ruoff. Evolution of graphene growth on ni and cu by carbon isotope labeling. *Nano letters*, 9(12):4268–4272, 2009.
- [51] H Kim, C Mattevi, M R Calvo, J C Oberg, L Artiglia, S Agnoli, C F Hirjibehedin, M Chhowalla, and E Saiz. Activation energy paths for graphene nucleation and growth on cu. *ACS nano*, 6(4):3614–3623, 2012.
- [52] E L Pang, N Q Vo, T Philippe, and P W Voorhees. Modeling interface-controlled phase transformation kinetics in thin films. *Journal of Applied Physics*, 117(17):175304, 2015.
- [53] M M Moghadam and P W Voorhees. Thin film phase transformation kinetics: From theory to experiment. *Scripta Materialia*, 124:164–168, 2016.

- [54] C S Ganpule, A L Roytburd, V Nagarajan, B K Hill, S B Ogale, E D Williams, R Ramesh, and J F Scott. Polarization relaxation kinetics and 180 domain wall dynamics in ferroelectric thin films. *Physical Review B*, 65(1):014101, 2001.
- [55] Z J Liu, J Ouyang, W Zhou, and X D Wang. Numerical simulation of the polymer crystallization during cooling stage by using level set method. *Computational Materials Science*, 97:245–253, 2015.
- [56] X Wang, Q Yuan, J Li, and F Ding. The transition metal surface dependent methane decomposition in graphene chemical vapor deposition growth. *Nanoscale*, 9(32):11584–11589, 2017.
- [57] K Celebi, M T Cole, J W Choi, F Wyczisk, P Legagneux, N Rupesinghe, J Robertson, K B K Teo, and H G Park. Evolutionary kinetics of graphene formation on copper. *Nano Letters*, 13(3):967–974, 2013.
- [58] M H Zwietering, I Jongenburger, F M Rombouts, and K van 't Riet. Modeling of the bacterial growth curve. *Applied and Environmental Microbiology*, 56(6):1875–1881, 1990.
- [59] B Gompertz. Xxiv. on the nature of the function expressive of the law of human mortality, and on a new mode of determining the value of life contingencies. in a letter to francis baily, esq. f. r. s. &c. *Philosophical Transactions of the Royal Society of London*, 115:513–583, 1825.
- [60] M Y A Shukor. Evaluation of several mathematical models for fitting the growth of the algae *dunaliella tertiolecta*. *Asian Journal of Plant Biology*, 2(1), 2014.
- [61] J Aroesty, T Lincoln, N Shapiro, and G Boccia. Tumor growth and chemotherapy: Mathematical methods, computer simulations, and experimental foundations. *Mathematical Biosciences*, 17(3):243 – 300, 1973.
- [62] D M. Easton. Gompertz kinetics model of fast chemical neurotransmission currents. *Synapse*, 58(1):53–61, 2005.
- [63] F C Figueira, N J Moura, and M B Ribeiro. The gompertz–pareto income distribution. *Physica A: Statistical Mechanics and its Applications*, 390(4):689 – 698, 2011.
- [64] C V Raman. A new radiation [reproduced from indian j. phys., 1928, 2, 387?398]. *Current Science*, 74(4):382–386, 1998.

- [65] D A Long. *Raman spectroscopy*. McGraw-Hill International Book Company, 1977.
- [66] H Barańska, A Łabudzińska, and J Terpiński. *Laser Raman spectrometry: analytical applications*. Ellis Horwood series in analytical chemistry. E. Horwood, 1987.
- [67] J M Hollas. *Modern Spectroscopy*. Wiley, 2004.
- [68] J R Ferraro and K Nakamoto. *Introductory Raman Spectroscopy*. Elsevier Science, 2012.
- [69] R L McCreery. *Raman Spectroscopy for Chemical Analysis*. Chemical Analysis: A Series of Monographs on Analytical Chemistry and Its Applications. Wiley, 2005.
- [70] C S S R Kumar. *Raman Spectroscopy for Nanomaterials Characterization*. Springer, 2012.
- [71] L M Malard, M A A Pimenta, G Dresselhaus, and M S Dresselhaus. Raman spectroscopy in graphene. *Physics Reports*, 473(5):51–87, 2009.
- [72] M S Dresselhaus, A Jorio, M Hofmann, G Dresselhaus, and R Saito. Perspectives on carbon nanotubes and graphene raman spectroscopy. *Nano letters*, 10(3):751–758, 2010.
- [73] A Bogner, P H Jouneau, G Thollet, D Basset, and C Gauthier. A history of scanning electron microscopy developments: towards “wet-stem” imaging. *Micron*, 38(4):390–401, 2007.
- [74] J Goldstein. *Practical scanning electron microscopy: electron and ion microprobe analysis*. Springer Science & Business Media, 2012.
- [75] W Zhou and Z L Wang. *Scanning microscopy for nanotechnology: techniques and applications*. Springer science & business media, 2007.
- [76] P J Goodhew, J Humphreys, and R Beanland. *Electron microscopy and analysis*. CRC Press, 2000.
- [77] J M Cowley. *Electron Diffraction Techniques*. Number 2 tom. in Electron Diffraction Techniques. International Union of Crystallography, 1992.
- [78] A J Schwartz, M Kumar, B L Adams, and D P Field. *Electron Backscatter Diffraction in Materials Science*. Routledge research global environmental change series. Springer US, 2000.

- [79] M Ohring. *The Materials Science of Thin Films*. Referex Engineering. Academic Press, 1992.
- [80] W Zhang, P Wu, Z Li, and J Yang. First-principles thermodynamics of graphene growth on cu surfaces. *The Journal of Physical Chemistry C*, 115(36):17782–17787, 2011.
- [81] X Sun, L Lin, L Sun, J Zhang, D Rui, J Li, M Wang, C Tan, N Kang, D Wei, H Q Xu, H Peng, and Z Liu. Low-temperature and rapid growth of large single-crystalline graphene with ethane. *Small*, pages 1702916–n/a, 2017. 1702916.
- [82] C Mattevi, H Kim, and M Chhowalla. A review of chemical vapour deposition of graphene on copper. *Journal of Materials Chemistry*, 21(10):3324–3334, 2011.
- [83] J E Proctor, D M Armada, and A Vijayaraghavan. *An Introduction to Graphene and Carbon Nanotubes*. CRC Press, 2017.
- [84] J V Pearce, V Montag, D Lowe, and W Dong. Melting temperature of high-temperature fixed points for thermocouple calibrations. *International Journal of Thermophysics*, 32(1-2):463–470, 2011.
- [85] C Kang D H Jung, J E Nam, H Jeong, and J S Lee. Surface diffusion directed growth of anisotropic graphene domains on different copper lattices. *Scientific reports*, 6, 2016.
- [86] P Trinsoutrot, C Rabot, H Vergnes, A Delamoreanu, A Zenasni, and B Causat. High quality graphene synthesized by atmospheric pressure cvd on copper foil. *Surface and Coatings Technology*, 230:87–92, 2013.
- [87] A Ibrahim, S Akhtar, M Atieh, R Karnik, and T Laoui. Effects of annealing on copper substrate surface morphology and graphene growth by chemical vapor deposition. *Carbon*, 94:369–377, 2015.
- [88] D H Jung, C Kang, J E Nam, J S Kim, and J S Lee. Size and density of graphene domains grown with different annealing times. *Bulletin of the Korean Chemical Society*, 34(11):3312–3316, 2013.
- [89] Z Han, A Kimouche, D Kalita, A Allain, H Arjmandi-Tash, A Reserbat-Plantey, L Marty, S Pairis, V Reita, N Bendiab, et al. Homogeneous optical and electronic properties of graphene due to the suppression of multilayer patches during cvd on copper foils. *Advanced Functional Materials*, 24(7):964–970, 2014.

- [90] P O'Brien, N L Pickett, and D J Otway. Developments in cvd delivery systems: A chemist's perspective on the chemical and physical interactions between precursors. *Chemical Vapor Deposition*, 8(6):237–249, 2002.
- [91] H O Pierson. *Handbook of Chemical Vapor Deposition, 2nd Edition: Principles, Technology and Applications*. Materials Science and Process Technology. Elsevier Science, 1999.
- [92] Vecstar Ltd. Installation, operation & maintenance instructions for types vctf1. 2017.
- [93] West control solutions. Users manual for cal 9500p programmable process controller. 2016.
- [94] For more information on the ASEQ Rm1 Raman spectrometer see. [http://www.aseq-instruments.com/rm1\\_spec\\_full.pdf](http://www.aseq-instruments.com/rm1_spec_full.pdf).
- [95] FEI. Helios nanolab 600i datasheet. 2014.
- [96] Oxford Instruments Analytical. Nordlys400 datasheet. 2007.
- [97] For more information on the Tango and Mambo software see. <https://www.oxford-instruments.com/products/microanalysis/ebsd/ebsd-post-processing-software>.
- [98] L Fan, K Wang, J Wei, M Zhong, D Wu, and H Zhu. Correlation between nanoparticle location and graphene nucleation in chemical vapour deposition of graphene. *Journal of Materials Chemistry A*, 2(32):13123–13128, 2014.
- [99] S M Kim, A Hsu, Y H Lee, M Dresselhaus, T Palacios, K K Kim, and J Kong. The effect of copper pre-cleaning on graphene synthesis. *Nanotechnology*, 24(36):365602, 2013.
- [100] A T Murdock, C D van Engers, J Britton, V Babenko, S S Meysami, H Bishop, A Crossley, A A Koos, and N Grobert. Targeted removal of copper foil surface impurities for improved synthesis of cvd graphene. *Carbon*, 122:207–216, 2017.
- [101] L Gan and Z Luo. Turning off hydrogen to realize seeded growth of subcentimeter single-crystal graphene grains on copper. *Acs Nano*, 7(10):9480–9488, 2013.
- [102] G H Han, F Gunes, J J Bae, E S Kim, S J Chae, H J Shin, J Y Choi, D Pribat, and Y H Lee. Influence of copper morphology in forming nucleation seeds for graphene growth. *Nano letters*, 11(10):4144–4148, 2011.

- [103] X Li, C W Magnuson, A Venugopal, R M Tromp, J B Hannon, E M Vogel, L Colombo, and R S Ruoff. Large-area graphene single crystals grown by low-pressure chemical vapor deposition of methane on copper. *Journal of the American Chemical Society*, 133(9):2816–2819, 2011.
- [104] T J Gnanaprakasa, Y Gu, S K Eddy, Z Han, W J Beck, K Muralidharan, and S Raghavan. The role of copper pretreatment on the morphology of graphene grown by chemical vapor deposition. *Microelectronic Engineering*, 131:1–7, 2015.
- [105] M I Kairi, M Khavarian, S A Bakar, B Vigolo, and A R Mohamed. Recent trends in graphene materials synthesized by cvd with various carbon precursors. *Journal of Materials Science*, 53(2):851–879, 2018.
- [106] Y C Shin and J Kong. Hydrogen-excluded graphene synthesis via atmospheric pressure chemical vapor deposition. *Carbon*, 59:439–447, 2013.
- [107] E H Martins Ferreira, M V O Moutinho, F Stavale, M M Lucchese, R B Capaz, C A Achete, and A Jorio. Evolution of the raman spectra from single-, few-, and many-layer graphene with increasing disorder. *Phys. Rev. B*, 82:125429, Sep 2010.
- [108] C Casiraghi, S Pisana, K S Novoselov, A K Geim, and A C Ferrari. Raman fingerprint of charged impurities in graphene. *Applied Physics Letters*, 91(23):233108, 2007.
- [109] A C Ferrari and D M Basko. Raman spectroscopy as a versatile tool for studying the properties of graphene. *Nature nanotechnology*, 8(4):235, 2013.
- [110] M J Starink. On the meaning of the impingement parameter in kinetic equations for nucleation and growth reactions. *Journal of Materials Science*, 36(18):4433–4441, 2001.
- [111] K Hayashi, S Sato, and N Yokoyama. Anisotropic graphene growth accompanied by step bunching on a dynamic copper surface. *Nanotechnology*, 24(2):025603, 2012.
- [112] M A Van Hove and G A Somorjai. A new microfacet notation for high-miller-index surfaces of cubic materials with terrace, step and kink structures. *Surface Science*, 92(2-3):489–518, 1980.